

Copyright

by

Joshua Christopher Bautista-Anguiano

2016

**The Report Committee for Joshua Christopher Bautista-Anguiano
Certifies that this is the approved version of the following report:**

**Modeling, Simulation and Interpretation of Spontaneous Potential Logs
to Quantify Hydrocarbon Saturation**

**APPROVED BY
SUPERVISING COMMITTEE:**

Supervisor:

Carlos Torres-Verdín

Maša Prodanović

**Modeling, Simulation and Interpretation of Spontaneous Potential Logs
to Quantify Hydrocarbon Saturation**

by

Joshua Christopher Bautista-Anguiano, B.S.

Report

Presented to the Faculty of the Graduate School of

The University of Texas at Austin

in Partial Fulfillment

of the Requirements

for the Degree of

Master of Science in Engineering

The University of Texas at Austin

December, 2016

Dedication

Dedicated to my parents, to my wife, to my siblings and to all the silent friends who have been my daily witnesses.

Acknowledgements

Although this report is an intermediate step towards pursuing my Ph.D., I wish to sincerely thank my supervisor, Dr. Carlos Torres-Verdín, for his endless patience and enlightenment after every weekly discussion I have had with him in the last 3 years. No one else in my life has made me grow as much, both intellectually and as a person.

I also thank Reynaldo Casanova for his impeccable logistical support during this time. Many thanks go to him for all his advice and guidance through UT's complex administrative system.

Thanks to Dr. Prodanović, whose advice was very useful and made my research a more interesting and productive activity than I could have imagined. Thank you for all the 15-minute discussions we had, and thanks for your guidance and support.

My peers in the research group were always very supportive. Thanks to Mauro Palavecino, Juan Diego Escobar Gomez, Colin Schroeder, Mathilde Luycx, Elsa Maalouf, Wilberth Herrera, David Medellin, David Gonzalez, Mohammed Albusairi, Vivek Ravi, Ayaz Mehmani, Hyungjoo Lee and Mohammed Bennis. Also thanks go to those who have graduated and left the research group, but whose support was important as well. Shaina Kelly, Paul Sayar and Siddharth Mishra, thank you to the three of you for all the advice and help you gave me during my first days in Graduate School. To Roger Terzian, Joaquin Ambia-Garrido and Bruce Klappauf, thank you for your support with UTAPWeLS.

Finally, thanks to Joachim Strobel from Wintershall for his constant support, inspiring discussions and for the field data included in this report.

Abstract

Modeling, Simulation and Interpretation of Spontaneous Potential Logs to Quantify Hydrocarbon Saturation

Joshua Christopher Bautista-Anguiano, M.S.E.

The University of Texas at Austin, 2016

Supervisor: Carlos Torres-Verdín

The Spontaneous Potential (SP) log has served for decades as a borehole correlation log and, under favorable circumstances, for the reliable in-situ assessment of water resistivity in rock formations of interest. Nevertheless, it is known from laboratory and field measurements that SP logs are sensitive to the presence of hydrocarbons. This report introduces the principles of SP log modeling using a mechanistic approach and describes their implementation in a SP log numerical simulator. Various synthetic and field cases verify the capabilities and improvement due to numerical modeling in the interpretation of SP logs. Quantification of hydrocarbon pore volume from SP logs is currently being validated with laboratory experiments. Those results and any modification to the models introduced in this document will be reported in a future doctoral dissertation.

The main contribution and conclusions from this thesis originate from the presence of the electrical double layer (EDL) on the surface of mineral grains, its impact on SP measurements in the presence of hydrocarbons, and the utility and limitations it poses for the calculation of hydrocarbon pore volume and porosity. These petrophysical properties are independent of size. Thus, pore-size distribution and the volume of influence of the

EDL in the pore space both determine whether SP logs will capture valuable information about hydrocarbon pore volume.

Field cases are presented in which quantification of hydrocarbon pore volume is possible. Simulations made using the mechanistic principles presented in this work show consistency both in modeling and in comparison to measurements at the borehole scale. These field cases consider both water- and hydrocarbon-bearing formations in distinct petrophysical and geological environments. Calculations of hydrocarbon saturation and porosity are verified by the use of porosity and resistivity logs.

The theory and results reported in this research highlight the importance of the EDL and the strong impact EDL has on improving interpretation of SP logs. Petrophysicists benefit from the possibility of mechanistically simulate SP logs that indicate the presence of hydrocarbon pore volume. This capability is useful in cases such as fresh-water environments where interpretation of resistivity logs may be problematic, or in mature hydrocarbon fields where only SP logs are available to the interpreter. The ability to simulate SP logs, particularly in mature hydrocarbon fields, offers a faster and less expensive way to evaluate new or overlooked gas or oil reservoirs.

Table of Contents

Dedication.....	iv
Acknowledgements.....	v
Abstract.....	vi
Table of Contents.....	viii
List of Tables.....	xi
List of Figures.....	xii
CHAPTER 1: INTRODUCTION.....	1
1.1 Historical background.....	1
1.2 Motivation.....	2
1.3 Expectation from this work.....	4
1.4 Organization of this report.....	4
CHAPTER 2: THEORETICAL FRAMEWORK.....	6
2.1 Fick's equations of mass transport.....	6
2.2 Coupled fluxes.....	7
2.3 Components of the Spontaneous Potential log.....	9
2.3.1 Membrane potential.....	9
2.3.2 Liquid-junction potential.....	10
2.3.3 Streaming potential.....	11
2.4 Electrical Double Layer.....	12
2.5 Total flux at steady state.....	17
2.5.1 Null divergence of the total flux vector.....	18
CHAPTER 3: PETROPHYSICS OF SPONTANEOUS POTENTIAL LOGS.....	20
3.1 Spontaneous potential currents.....	20
3.2 Dependence of spontaneous potential on conductivity.....	22
3.3 Factors affecting spontaneous potential logs.....	22
3.4 Measuring SP in the borehole.....	24

3.4.1 Sandstone and shale baselines	25
3.5 Geometrical aspects	28
3.6 Petrophysical theory of SP	30
3.6.1 Electrochemical source under a petrophysical perspective	33
3.6.2 Electrokinetic source under a petrophysical perspective	38
CHAPTER 4: SIMULATION CODE	40
4.1 Discrete equations	40
4.1.1 Interblock properties	41
4.1.2 Discretization in each direction	42
4.2 Boundary conditions	43
4.3 Matrix entries	43
4.4 Iterative solution	44
4.5 Simulated SP log	46
4.6 Input source information	46
4.7 Algorithm performance	47
CHAPTER 5: SYNTHETIC CASES FOR NUMERICAL SIMULATION OF SP MEASUREMENTS	49
5.1 Simple synthetic cases	49
5.1.1 Bed thickness effect	52
5.1.2 Thick rock beds impermeable to ions and fluids	53
5.2 Shale effects	58
5.2.1 Simulation of different shale ion permeabilities	58
5.3 Hydrocarbon effects	60
5.3.1 Hydrocarbon effects on SP logs acquired across oil-wet rocks	63
5.4 SP log with different electrolytes	63
CHAPTER 6: FIELD EXAMPLES OF THE QUANTITATIVE INTERPRETATION OF SP LOGS VIA NUMERICAL SIMULATION	65
6.1 Field case examples	65
6.1.1 Oil-water contact detection from SP log	66
6.1.2 SP log across a continuous capillary transition of water saturation	66

6.2 Discussion	67
CHAPTER 7: CONCLUSIONS AND FUTURE WORK.....	70
7.1 Conclusions.....	70
7.2 Future work.....	73
List of symbols.....	74
List of acronyms	75
References.....	76
Vita	82

List of Tables

Table 2.1: Fluxes and driving forces. Each coupling phenomenon has a specific name, depending on the driving force and the transport phenomena it produces [adapted from (Mitchell, 1991)].	8
Table 3.1: Properties that affect the SP log in a borehole.....	23
Table 3.2: Values used for generating Figure 3.10.	38
Table 4.1: Summary of algorithm performance. CPU time indicates only the time necessary to obtain vector x by the bi-conjugate method. RAM memory is the total memory required for all the calculations in the algorithm. ...	48
Table 5.1: Numerical results obtained for a case in which the borehole mud and formation water exhibit the same water salinity. The result is the same, regardless of the salinity of the shale beds that shoulder the permeable bed. SP is measured as the deflection from the shale baseline. A zero SP indicates that no deflection occurs along the permeable bed.....	51
Table 5.2: Properties assumed for calculating effective ion diffusivities for the numerical simulation of SP log shown in Figure 5.10.....	63

List of Figures

- Figure 2.1: Two containers develop a diffusion potential because of differences in salt concentration and differences in the average velocity of the ions involved. Sizes of the ions above indicate their relative ionic radii. In reality, each ion in solution possesses a shell of water (not shown), which makes Na^+ slower than Cl^- [reproduced from Ellis and Singer, 2007].9
- Figure 2.2: Stern and diffusive layers. Ions in solution are shown without their hydration shell to simplify the figure [reproduced from Thanh and Sprik, 2016].13
- Figure 2.3: Coion and counterion concentration as a function of distance from the mineral surface [reproduced from Winsauer and McCardell, 1953].13
- Figure 3.1: SP currents as conceived by H.G. Doll. These currents complete a closed circuit in the borehole and in the rock beds [reproduced from Doll, 1949].20
- Figure 3.2: Insulating plug that opens the electrical circuit conceived by H.G. Doll, and which, in theory, would not allow the flow of SP currents [reproduced from Doll, 1949].21
- Figure 3.3: Illustration of the basic SP equipment. Electrode N is the reference electrode, while electrode M is the moving electrode in the borehole. Differences of electric potential between these electrodes are the basis of the conventional SP log [reproduced from Doll, 1949].24
- Figure 3.4: Shale (right) and sandstone (left) baselines as dashed lines on the first track [reproduced from Doll, 1949].26

Figure 3.5: Shale baseline shifting in two field examples [reproduced from Doll, 1949].	27
Figure 3.6: Normalized SP as a function of normalized thickness. A 100% SP indicates that the maximum SP is attained across the rock bed for any given salinity ratio and temperature.	28
Figure 3.7: Effect of dip on SP logs for a thin and a thick bed for a dip of 0 and 45 degrees for a 3-layered synthetic model. In Track (a) the SP amplitude is smaller than in track (b), corresponding to their effective dip thickness. The logs present in tracks (a) and (b) are: gamma-ray (green, dashed), SP for horizontal beds (red), and SP for dipping beds (purple). Bed boundaries are shown as blue dashed horizontal lines.	31
Figure 3.8: Effective dip thickness for beds of different thickness and dip in different boreholes, following Equation 3.2.	32
Figure 3.9: Bundle of capillary tubes for a representative elementary volume. These tubes are independent of each other, not crossing or communicating among themselves. The dark blue region corresponds to the EDL zone (not to scale), while the clear blue region is the bulk region, where bulk solution properties dominate.	33
Figure 3.10: Effect of water saturation on the normalized SP for different values of $S_{w,EDL}$: 0.01 (red), 0.05 (blue), and 0.08 (green). In (a) there is no diffusivity improvement for cations in the EDL. In (b) the diffusivity of cations in the EDL is ten times higher than in the bulk solution (see Table 3.2).	37

Figure 3.11: SP coefficient [$K = RF^{-1}(t_{Na} - t_{Cl})$] and capillary pressure as a function of water saturation. In both curves, a decrease in the water saturation corresponds to an increase in both capillary pressure and SP magnitude [reproduced from McCall et al. (1971)].....	38
Figure 4.1: Structures of matrix A and vector x used to simulate SP logs.	45
Figure 4.2: The SP log at the borehole's axis (yellow dot), at each depth, is calculated as the arithmetic average of the values of electric potential of gridpoints surrounding the origin (shown in blue) because no SP sources exist inside the borehole (see text above). The borehole is in blue and the formation is in yellow. Red dots represent the gridpoints that are not the first gridpoints in the r-direction.	47
Figure 5.1: Comparison between theoretical SP values (solid line) and results from numerical simulations (dots) for a thick, clean-water-bearing horizontal rock bed penetrated by a vertical well with a 0.1 m radius. The temperature is set to 50 °C. Shale beds are assumed to be perfect semi-permeable membranes.	50
Figure 5.2: Comparison between results of increasing the original wellbore radius, r_o , of 0.1 m (dots) and mud-filtrate invading by the same length, keeping r_o unaltered (dashed line). The salinity ratio and temperature for generating this figure are 10 and 50 °C.	50

Figure 5.3: Track (a): SP log simulated on different days after the onset of mud-filtrate invasion shown on the first track. The SP simulator can take the radial distribution into account and calculate the electrochemical SP log. Shales are assumed to be perfect semi-permeable membranes. The temperature is set to 122 °F. The salinity ratio for this example is 15. The borehole has a radius of 10 cm. All layers are water-bearing. Track (b): Salt concentration profile on that corresponds to mud-filtrate invasion after 15 days.54

Figure 5.4: Track (a): Comparison of the SP log simulated across permeable beds with only a difference in their thickness. A comparison of the SP at 0 and 1 day after the onset of mud-filtrate invasion is presented to emphasize that invasion mainly affects the thinnest beds. Borehole size is 10 cm. Mud and formation water salinity are 3 kppm and 15 kppm. Temperature is set to 122 °F. Shales beds are perfect semi-permeable membranes. The second track shows the radial salinity profile after 1 day of invasion. All beds are water-bearing. Track (b): Salt concentration profile on that corresponds to mud-filtrate invasion after 1 day.55

Figure 5.5: Averaging of SP log for thin-bedded formations. For the red SP log, the shale and non-shale beds are each 1 m thick, while for the purple SP log, the beds are each 10 cm thick. Both SP logs assume negligible mud-filtrate invasion. The temperature is set to 115 °F. All shale beds are assumed as perfect semi-permeable membranes. Borehole size is 10 cm. Mud and formation water salinity are 3 kppm and 15 kppm. All layers are water-bearing.56

- Figure 5.6: SP logs for different shale and sandstone configurations. A thick non-porous bed is located between 1,104 and 1,126 m in all configurations. Regardless of the arrangement of shale and sandstone beds, the SP log across the thick bed remains the same, which can be taken as an absolute baseline, given that no salt exchange occurs through it. All porous beds are water-bearing. The temperature is set to 122 °F. Mud salinity is 5 kppm and formation water salinity is 50 kppm in all cases. All examples assume no mud-filtrate invasion.57
- Figure 5.7: SP log calculated from individual non-shale and shale layers (purple log), and SP calculated from Eq. 3.4 for an effective medium (red log). As the thickness of individual layers decreases, the measured log converges to the effective log in red. The temperature is set to 122 °F. Mud salinity and formation water salinity are 5 kppm and 50 kppm, respectively. The borehole size is 10 cm. All layers are water-bearing only and assume no mud-filtrate invasion.59
- Figure 5.8: Normalized SP as a function of shale fraction (C_{sh}) for dispersed (red line) and laminated (blue line) shale topologies. The example plotted considers a rock with non-shale porosity of 0.3 and shale porosity of 0.15. In both cases, the relationship can be nonlinear with respect to C_{sh} . The calculations assume no mud-filtrate invasion.60

Figure 5.9: SP log for a non-shale porous bed rock shouldered by two different shale beds. The upper shale layer is simulated as a perfect semi-permeable membrane, while the lower shale layer is either as a highly laminated sandstone-shale sequence, a fractured shale, or a shale with different composition from the upper shale. Temperature is set to 122 °F. Mud and formation water salinities are 5 kppm and 50 kppm, respectively. For this figure, the transport numbers of sodium for the upper and lower shales are 1 and 0.8, respectively. All layers are only water-bearing and assume no mud-filtrate invasion.61

Figure 5.10: Track (a): Numerically simulated SP log with presence of hydrocarbon. The temperature is set to 120 °F. The mud and formation water salinities are 5 kppm and 50 kppm, respectively. Shales at the top and at the bottom are perfect semi-permeable membranes. The SP log is simulated with a mud-filtrate invasion time of 12 hours. The borehole radius is 10 cm. Track (b): Radial and vertical water-saturation distribution.62

Figure 6.1: Track (a): Gamma-ray log in green, SP log in purple, and the numerically simulated SP log in red. The numerically simulated SP agrees with the SP log from the field. To achieve the match of the SP logs, the simulator used the properties $S_{w,EDL} = 0.05$, $D_{Na,EDL} = 8 \times 10^{-5} \text{ cm}^2/\text{s}$, and $D_{Cl,EDL} = 1 \times 10^{-10} \text{ cm}^2/\text{s}$ in the bed that extends from XX360 to XX405 ft. Track (b): Resistivity logs. Track (c): Density (green) and neutron (purple) logs. The neutron log is in limestone units. Track (d): Radial and vertical water-saturation distribution.68

Figure 6.2: Track (a): Gamma-ray log with its simulated counterpart, both in green, and SP log in purple with the numerically simulated SP log in red. To achieve the match of the SP logs, the simulator used the properties $S_{w,EDL} = 0.05$, $D_{Na,EDL} = 8 \times 10^{-5} \text{ cm}^2/\text{s}$, and $D_{Cl,EDL} = 1 \times 10^{-10} \text{ cm}^2/\text{s}$ in the reservoir that extends from 1012 to 1021 m. Track (b): Resistivity logs (solid lines) and their simulated counterparts (dotted lines). Deep resistivity is in red, while shallow resistivity is in blue. Track (c): Density log in red and neutron log in blue. The numerical simulations of both logs are shown with dotted lines. The neutron log is in limestone units. Tracks (d), (e), and (f) are the resistivity, water saturation, and salt concentration radial profiles, respectively.....69

CHAPTER 1: INTRODUCTION

1.1 HISTORICAL BACKGROUND

Borehole spontaneous potential (SP) logs have been acquired since the first measurements made by the Schlumberger brothers and H.G. Doll (Schlumberger *et al.*, 1934). This phenomenon, although accidentally discovered, has provided petrophysicists with a valuable tool for the identification of permeable and impermeable layers before the development of more advanced measurement techniques such as gamma-ray logging. Several later authors (De Andrade, 1955; Dickey, 1944; Doll, 1949; Kerver and Prokop, 1957; McCardell *et al.*, 1953; Mounce and Rust, 1944; Wyllie, 1949; Wyllie and Southwick, 1954) have also attempted to explain the physical origins of the SP log.

Doll (1949) established the basic physical and interpretation principles of SP logs that have been followed until the present. Later studies derived from Doll's (1949) work provided a general method for explaining the effect of hydrocarbon pore volume on SP measurements (Kerver and Prokop, 1957; Ortiz *et al.*, 1972; Poupon *et al.*, 1954; Revil, 1999). However, most of these explanations emanated from a macroscopic perspective, with little or no regard to the pore level properties of the rocks, except when considering clay fraction (Doll, 1949, 1950). Attempts following Archie's equation (Poupon *et al.*, 1954) were not widely applicable for locating and quantifying hydrocarbon pore volume because the petrophysical understanding from that time was not yet fully developed.

Based on experimental work by different authors (Kerver and Prokop, 1957; McCall *et al.*, 1971; Ortiz *et al.*, 1972; Revil, 1999), it has been verified in many studies that presence of hydrocarbons has an impact on SP readings. However, these studies lack a consistent physical model. Although some authors (Lehikoinen *et al.*, 1999; Ortiz *et al.*, 1972; Revil *et al.*, 1998) state that presence of clay minerals is necessary for hydrocarbons

to have a measurable impact on SP logs, results from other publications (Kerver and Prokop, 1957; McCall *et al.*, 1971) disprove the need for clay minerals, indicating that even in clean formations, the effect of hydrocarbons on SP measurements can be observed in some cases.

Currently, SP logs are not commonly measured because of the introduction of oil-based muds and because of the availability of more sophisticated logging tools to evaluate rock formations. Because of these circumstances, when an SP log is measured by a service company, it is usually done without any financial charge because it is considered useless in the quantification of hydrocarbons. If, however, SP logs were more commonly included in the formation evaluation process, they would add value to the information available, and they would be provided free of charge by the service company that made the measurement.

1.2 MOTIVATION

In many instances it is impossible to re-log many wells that have been producing hydrocarbons for decades, thus leaving petrophysicists with only the SP and old-generation gamma-ray, resistivity laterolog, or neutron porosity logs. Contrary to SP tools and logging techniques, gamma-ray, resistivity and neutron tools and acquisition methods have evolved significantly through the 20th century. No such significant improvement in the SP log has taken place, leaving most of our understanding to the incomplete theoretical framework from the 1940's and 1950's when SP interpretation was done on a daily basis. Because the SP log is the oldest and most widespread log in most, if not all, mature fields around the world, it is particularly important to deepen the knowledge of SP phenomena to take advantage of the information this log provides.

In many cases no or only one resistivity curve is available, without access to a porosity curve to assess whether the changes in resistivity come from a change in porosity,

changes in water salinity, or presence of hydrocarbons. Given that the SP has marginal sensitivity to changes in porosity (Doll, 1949), and with an appropriate calibration, the SP log could help petrophysicists to discover reservoirs overlooked in the past and at a low financial cost. On the other hand, even with a set of resistivity curves, using the SP log in freshwater environments has its advantages. Interpretation of resistivity logs is generally limited to cases where the reservoir water is salty enough to allow the application of all well-known models of water saturation (Archie, 1942; Clavier *et al.*, 1984; Juhasz, 1981). This is not the case for the SP log, which is known to be sensitive to hydrocarbon pore volume in both brine- and freshwater-bearing rocks.

The mechanistic modeling and the development of a simulator can, in the future, aid in the estimation of water saturation from SP logs. However, without a consistent physical model that allows the quantification of hydrocarbon pore volume, research is needed to complement this deficiency in the general understanding of SP phenomena. Once it is possible to take into account all geometric and petrophysical variables involved in SP logs, the possibility of inversion of SP logs could become attractive. In mature fields, this represents a low-cost option that could significantly increase current estimated reserves.

From a more academic point of view, future research undertaken on SP logs will facilitate verifying or discrediting previous work on this topic; our understanding of physics and petrophysics has increased since earlier attempts by petrophysicists to understand the physics behind the SP log (Doll, 1949; Hill and Milburn, 1956; McCardell *et al.*, 1953; Mounce and Rust, 1944; Wyllie, 1949). Central to this report is the presence of the electrical double layer (EDL) on grains that compose reservoir rocks. Commonly ignored, the EDL is what defines the sensitivity of a rock to the presence of hydrocarbons in an SP curve. Thus, better understanding of the conditions where the EDL governs the SP log in the presence of hydrocarbons is desirable.

1.3 EXPECTATION FROM THIS WORK

It is widely known that SP logs result from electrochemical and electrokinetic phenomena. In this work, most of the discussion and results presented in the following chapters are heavily centered on the electrochemical origin of the SP log.

1.4 ORGANIZATION OF THIS REPORT

Chapter 2 focuses on theoretical aspects of SP phenomena, introducing the reader to basic concepts of mass diffusion, coupled fluxes, zeta potential, and EDL thickness, among others. These concepts are the basic physical principles used in the SP simulator introduced in Chapter 4.

Chapter 3 presents and discusses geometrical and petrophysical factors that are known to have a direct and important impact on SP logs. This chapter introduces models that describe diffusion in porous media and examines how the presence of the EDL can alter the sensitivity of SP logs to the content of hydrocarbons.

Chapter 4 presents the numerical algorithm of the SP numerical simulator. All discrete equations, boundary conditions, and solving methods are shown, but no computer code is provided with this report. CPU time and RAM requirements for SP log numerical simulation in a multi-layer example appears at the end of this chapter.

Chapter 5 contains several synthetic cases to illustrate the concepts and discussion from Chapters 2 and 3. All these synthetic cases were calculated from the SP numerical simulator described in Chapter 4.

Chapter 6 shows two field cases where all logs, including SP logs, have been matched in the presence of hydrocarbon. Hydrocarbon pore volume calculated from SP logs agrees with that calculated from porosity and resistivity logs.

Chapter 7 reports the conclusions from this report, details pending work on SP research, and suggests further steps toward improving the estimation of hydrocarbon pore volume from SP logs.

CHAPTER 2: THEORETICAL FRAMEWORK

This chapter introduces the reader to the basic physical concepts behind SP phenomena. It also presents mathematical models that describe mass diffusion and discusses how these models can be extended to describe coupled fluxes. This chapter ends with a brief discussion of the electrical double layer (EDL) and basic equations that macroscopically describe electrochemical and electrokinetic components of SP logs at steady state.

2.1 FICK'S EQUATIONS OF MASS TRANSPORT

Mass transport is generally described by Fick's equations,

$$\bar{j}_i = -D\nabla c_i, \quad (2.1)$$

$$\frac{\partial c_i}{\partial t} + \nabla \cdot \bar{j}_i = 0, \quad (2.2)$$

where Equation 2.1 indicates that, for component i , a gradient in concentration, c_i , is directly proportional to \bar{j}_i , mass flux (usually given in terms of mole/m²·s or kg/m²·s). Mass flux and concentration gradient are related by parameter D , known as mass diffusivity. On the other hand, Equation 2.2, relates \bar{j}_i to change rate in time in concentration of component i . Equation 2.2 assumes that no chemical reaction occurs, which makes it directly equivalent to the law of conservation of mass.

Fick's equations can be successfully applied, except for some particular situations (Bringuier, 2013; Krishna and van Baten, 2009; Krishna and Wesselingh, 1997), to describe mass transport in dilute solutions. In more concentrated solutions, instead of using

the concentration of substance i , its activity, a_i , is employed (Koryta *et al.*, 1994; Krishna and Wesselingh, 1997). This description for mass transport is only applicable, nevertheless, to neutral particles, particles with a net charge equal to zero. In the case of ion transport, as in the SP phenomena, the charge inherent to all ions plays an important role in their transport. In this case, ion transport originates from coupled fluxes, deviating from the conventional Fick's equations.

2.2 COUPLED FLUXES

Coupled fluxes are the result of different physical forces participating in the same transport process. Retaking the mass transport from Section 2.1, we know that when particles are electrically charged, as in an electrolyte, a concentration (activity) gradient results in a net mass flux of ions. For this example, let us assume that we have two containers with the same electrolyte at different concentrations, as depicted in Figure 2.1. When allowed to communicate with each other, the concentration gradient will result in ions moving from the container with the highest concentration to that with lower concentration. If this electrolyte contained Na^+ and Cl^- ions, then both ions would flow in the same direction because of their individual concentration gradients. It is known, however, that anions and cations do not diffuse at the same rate (Ellis and Singer, 2007; Revil, 1999); the Cl^- anions are slightly faster than Na^+ cations due to differences in the structure and thickness of the hydration layer associated with each ion in solution (Hamann *et al.*, 2007; Koryta *et al.*, 1994). A spatial separation of Cl^- and Na^+ occurs, giving rise to a non-zero net electrical potential gradient. Cations will flow from the high to low electrical potential zones, while the anions will flow in opposite direction. In this case, we observe that because of a concentration and an electrical potential gradient, ion fluxes ensue. The flux generated from the electric potential gradient is coupled with that produced by the

differences in concentration. Sill (1983) explains how the primary flux (mass flux) can produce a secondary flux (charge flux). Generally speaking, it could be stated that all types of fluxes can originate not only from their classical definition (as Fick's equations, in the example), but also from other driving forces because the physical elements (ions, in this case) possess more than one physical property changing due to the primary flux. Table 2.1 is a summary of many well-known fluxes and forces. The elements on the main diagonal are the primary fluxes, while the rest are secondary or coupled fluxes.

Driving Flux \ Force	Chemical potential	Fluid pressure	Temperature	Electric potential
Solute flux	Mass diffusion	Salt advection	Soret effect	Electrophoresis
Volumetric flux	Osmosis	Fluid advection	Thermo- osmosis	Electro- osmosis
Heat flux	DuFour effect	Heat advection	Heat diffusion	Peltier effect
Current flux	Diffusion current	Streaming current	Thermo- electricity	Electric current

Table 2.1: Fluxes and driving forces. Each coupling phenomenon has a specific name, depending on the driving force and the transport phenomena it produces [adapted from Mitchell, 1991].

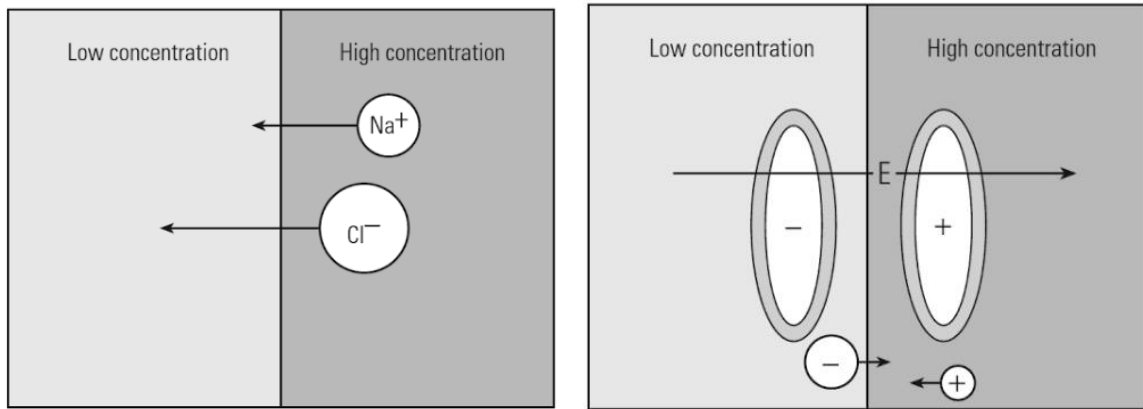


Figure 2.1: Two containers develop a diffusion potential because of differences in salt concentration and differences in the average velocity of the ions involved. Sizes of the ions above indicate their relative ionic radii. In reality, each ion in solution possesses a shell of water (not shown), which makes Na^+ slower than Cl^- [reproduced from Ellis and Singer, 2007].

2.3 COMPONENTS OF THE SPONTANEOUS POTENTIAL LOG

Spontaneous potential logs are known to originate from three different sources: a membrane potential, a liquid-junction potential, and a streaming potential (Doll, 1949; Ellis and Singer, 2007). Each is the result of a different transport mechanism, but they all involve coupled fluxes. In Table 2.1, the electrochemical component originates from the coupling of chemical and electric potentials to yield a net ionic current flux, whereas the streaming potential results from the coupling of the electric potential and pressure to yield also a net ionic current flux.

2.3.1 Membrane potential

When two containers are separated by a semi-permeable membrane that only allows cations to diffuse through it, a coupled flux arises from the separation of cations and anions. The electric potential difference that arises between each side of the membrane to

compensate for the diffusion of cations in the membrane is known as the membrane potential. The membrane (Nernst) potential is expressed in differential form as,

$$\nabla V = -\frac{RT}{F} \nabla \ln \left(\frac{c^I}{c^{II}} \right), \quad (2.3)$$

where V is electric potential, R is universal gas constant, T is absolute temperature, F is Faraday's constant and c^I and c^{II} are the ion concentrations in each of the containers (Ellis and Singer, 2007; Revil, 1999). Equation 2.3 describes a perfect semi-permeable membrane.

The membrane (or Nernst) potential is the highest electric potential difference that can exist across a semi-permeable membrane located between two containers that have different concentrations of the same electrolyte. If only anions are allowed to pass, the potential difference between both containers is the same in magnitude, but with the opposite sign. In nature, it is more common to find rocks that are impermeable to anions. Equation 2.3 assumes that only a monovalent salt is present, that ion-ion interactions are negligible and that using concentration values instead of activity values is a valid approach. Such assumptions are made during the rest of this work.

2.3.2 Liquid-junction potential

The membrane potential is a special case of a membrane that only allows the passage of ions of one sign. On the other hand, the liquid-junction (diffusion) potential results from a medium that allow all ions to diffuse regardless of their electric charge sign, following a similar model to that of a perfect membrane, but with an additional factor known as the transport number difference (Ellis and Singer, 2007; Ortiz *et al.*, 1972; Revil, 1999; Revil *et al.*, 1998), as given by

$$\nabla V = -\frac{RT}{F} (t_{\text{cat}} - t_{\text{an}}) \nabla \ln \left(\frac{c^{\text{I}}}{c^{\text{II}}} \right), \quad (2.4)$$

where t_{cat} and t_{an} are the cation and anion transport numbers, respectively, for a monovalent salt. The transport number in Equation 2.4 is an important property inherent to each element ion, as it represents the fraction of the total mass/charge flux. If both transport numbers are equal, that indicates that no electrical potential gradient will exist, even if the concentration gradient is different from zero. Because, in this case, both ions contribute and displace at the same rate, no spatial separation occurs between them, resulting in a net zero electric potential gradient to compensate for charge separation. Transport numbers are defined as

$$t_j = \frac{D_j}{\sum_{k=1}^M D_k}, \quad (2.5)$$

where t_j and D_j are the transport number and the diffusivity constant for ion j , respectively, and M is the total number of ions in solution. Because of the definition in Equation 2.5, the sum of all transport numbers is always equal to one.

2.3.3 Streaming potential

Another mechanism (primary flux) that can result in a significant electrical potential difference is flow of water due to a pressure gradient. Even within an electrolyte body where no concentration (activity) gradients exists, a significant concentration gradient can exist close to liquid/solid interfaces, regardless of the solid being a mineral or plastic matrix. This concentration gradient occurs because of the existence of the Electrical Double Layer (EDL) at solid-liquid interfaces in porous media. Figure 2.2 introduces the

concept of zeta potential. The zeta potential is the electric potential at the shear plane, where the latter is an imaginary plane that separates the ions bound to the mineral surface from those that can diffuse.

Because of the existence of the EDL and fluid flow, the inlet of the medium where flow occurs finds itself depleted of counterions, while inside the porous medium (or at the outlet) an excess of counterions exists. To compensate for the rearrangement of charges promoted by fluid flow, an electrical potential gradient arises as a manner to redistribute the charges to return to the equilibrium state that existed before fluid flow took place. The relationship between the pressure gradient and the electric potential gradient at (quasi) steady state is

$$\nabla^2 V = -\nabla \cdot \left(\frac{k Q_v}{\mu \sigma} \nabla P \right), \quad (2.6)$$

where k is permeability, μ is fluid viscosity, σ is electrical conductivity of the porous medium and Q_v is charge density limited to the regions in the EDL that exists within the porous medium. Equation 2.6 is valid only under a zero-current condition in all the domain of interest.

2.4 ELECTRICAL DOUBLE LAYER

To extend the introduction of the EDL, this section is devoted to briefly describing the major characteristics of this small yet important spatial region inherent to all liquid-saturated porous media.

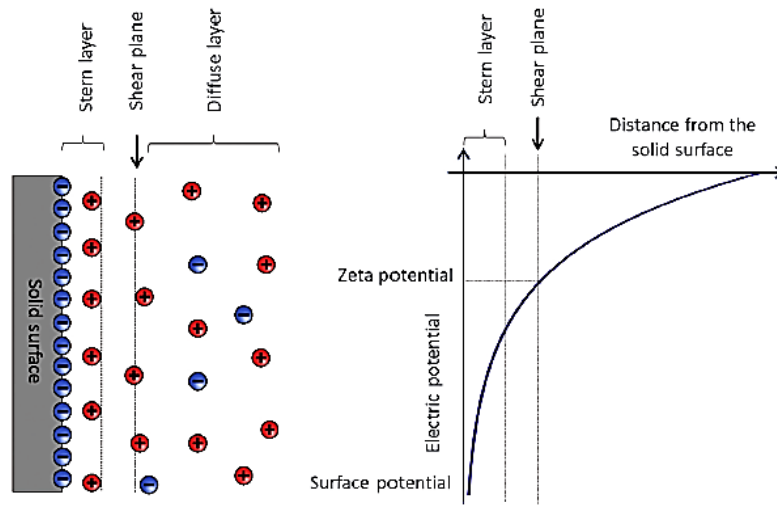


Figure 2.2: Stern and diffuse layers. Ions in solution are shown without their hydration shell to simplify the figure [reproduced from Thanh and Sprik, 2016].

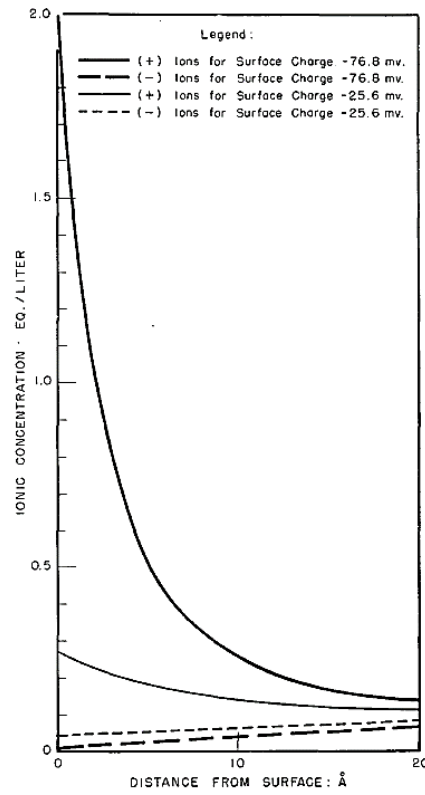


Figure 2.3: Coion and counterion concentration as a function of distance from the mineral surface [reproduced from Winsauer and McCardell, 1953].

The EDL results from uncompensated charges that occur on the surface of the solids in contact with fluids. In order to compensate for those charges, counterions (ions with opposite sign to that of the solid surface) accumulate on the surface and, in some cases, are adsorbed, to neutralize the surface charge. Because of thermal motion and remaining uncompensated charge on the surface, two main zones can be identified at the solid-liquid interface, the Stern and diffuse layers, from which the EDL received its name. Figure 2.3 shows how the counterion concentration increases exponentially (see Equation 2.7) as one approaches the grain surface, while the coion (ions with the same sign as the charged surface) concentration decreases. For the radial profiles in Figure 2.3, we assume a spherical particle of radius a with the origin of a spherical coordinate system at its center.

At electrochemical equilibrium, the concentration of coions and counterions at equilibrium follows a Boltzmann distribution. This distribution results independently from the shape of the interphase and is expressed as

$$c_{\pm}(\bar{r}) = c_f \exp\left(\mp \frac{zF\zeta(\bar{r})}{RT}\right), \quad (2.7)$$

where c_{\pm} is counterion/coion concentration as a function of position, \bar{r} , c_f is bulk concentration of ions, $\zeta(\bar{r})$ is electric potential as a function of position, and z is valence of ions involved. In Equation 2.7, as $\bar{r} \rightarrow \infty$, $\zeta(\bar{r}) \rightarrow 0$, so that a position away from the mineral surface counterion and coion concentrations are the same. Equation 2.7 is a well-established model, and its derivation is documented in literature on electrochemistry (Hamann *et al.*, 2007; Koryta *et al.*, 1994; Revil and Leroy, 2004).

The concept of zeta potential, $\zeta(\bar{r} \approx a)$, is central to the study of the EDL. The zeta potential determines the amount of uncompensated charge on the surface. A higher zeta potential both increases the concentration of counterions at the solid-liquid interface and

also affects the transport mechanisms whereby ion transport occurs. For example, when the size of pores is of the order of magnitude of the double layer, cations will be depleted, because depletion is the only way to allow for thermodynamic equilibrium inside the pore space, as explained in Daiguji (2010). This is the case in shales, which are known for being negatively charged on their solid surfaces, while impeding the path of anions, as this goes against the equilibrium requirements dictated by Equation 2.7.

The differential equation that describes the EDL potential is known as the Poisson-Boltzmann equation, as given by

$$\nabla^2 \zeta = \frac{2Fc_f}{\epsilon_f} \sinh\left(\frac{\zeta F}{RT}\right), \quad (2.8)$$

where ϵ_f is electrolyte dielectric constant. Equation 2.8 is a nonlinear differential equation, which can be linearized if the argument $\left|\frac{\zeta F}{RT}\right| \ll 1$, meaning that $\sinh(x) \approx x$. Equation 2.8 results from the combination of the Poisson's equation for electric potential and the Boltzmann's equation, which describes the distribution of the ions near the liquid-solid interface (Equation 2.7). Equation 2.8 is valid only for a monovalent salt (e.g., NaCl, KCl, KF).

Assuming that linearization is a valid approximation, Equation 2.8 can be rewritten as

$$\nabla^2 \zeta(\vec{r}) \approx \frac{2Fc_f}{\epsilon_f} \frac{F\zeta}{RT} = \kappa^2 \zeta, \quad (2.9)$$

where parameter $\lambda = \kappa^{-1}$, also known as the EDL thickness. The approximated Poisson-Boltzmann equation is known as the Debye-Hückel approximation.

The EDL thickness, defined as

$$\lambda = \sqrt{\frac{RT\epsilon_f}{2F^2c_f}}, \quad (2.10)$$

is not properly the thickness of the EDL, but rather is the distance at which the concentration of counterions has reduced by a factor $\exp(-1)$ compared to that at the solid surface. Equation 2.10 shows λ for a monovalent electrolyte.

A general expression for the EDL thickness for any valence, still assuming that the linear Poisson-Boltzmann equation is valid, is stated as

$$\lambda = \sqrt{\frac{RT\epsilon_f}{F^2 \sum_{i=1}^M z_i^2 c_{f,i}}}, \quad (2.11)$$

where $c_{f,i}$ is concentration of ion i in the bulk solution. It is important to note that the thickness decreases four times with divalent ions, compared to monovalent ions. This is an indication of the importance of knowing the electrolyte composition, as well as of understanding the mineral surface chemistry, which determines whether the linearization used is valid or not. An important aspect of this phenomenon is that both valence and concentration in the bulk have a direct impact on the size of the zone of influence of the EDL. In the following sections, the EDL thickness compared to the size of the pore is what all the three components of the spontaneous potential have in common. Despite their different physical origin, each component is affected directly by the influence of the EDL. This influence is what forms the physical foundation of the quantification of hydrocarbon pore volume based on the SP log.

Note that the electric potential in the Poisson-Boltzmann equation is not the same potential shown in the equations for spontaneous potential. Although related, the zeta potential is not measurable with the tools used for SP measurements because of its

nanometric nature. However, the zeta potential has a direct impact on the measurements with conventional SP equipment, which is the main motivation for developing a mechanistic model for SP numerical simulations.

2.5 TOTAL FLUX AT STEADY STATE

As described previously, different forces can originate the same kind of flux when such driving forces are coupled. We define the total flux as the sum of all the contributions from each force. From Woodruff et al. (2010),

$$\bar{j}_t = -\sigma \nabla V - \frac{kQ_v}{\mu} \nabla P - \frac{RT}{F} \sigma \sum_{i=1}^n \frac{t_i}{z_i} \nabla \ln c_i, \quad (2.12)$$

which describes total current in a general multi-ionic electrolyte. The linearity of Equation 2.12 is based on principles of irreversible thermodynamics, which assume a small departure from thermodynamic equilibrium locally.

When working with spontaneous potential, there is a transient period in which all the fluxes interact to counterbalance each other's effect. Although measurements could be done for this transient period, it occurs in a very small fraction of time; high-resolution devices used in the time domain are necessary to detect the change of V during this transition period. Hence, all spontaneous potential measurements are done in the quasi-steady state. Mathematically, the quasi-steady state implies that the divergence of \bar{j}_t is zero or negligible. No chemical reactions and no external sources of ions or of electrical potential are considered. Equation 2.12 thus contains only the terms of the primary and secondary fluxes; Sill (1983) provides practical examples of primary and secondary fluxes. It is assumed that the electrolyte contains only a monovalent salt to simplify the equations. Considering a null divergence for \bar{j}_t ,

$$\nabla \cdot \bar{j}_t = -\nabla \cdot \left(\sigma \nabla V - \frac{kQ_v}{\mu} \nabla P - \frac{RT}{F} \sigma \sum_{i=1}^n \frac{t_i}{z_i} \nabla \ln c_i \right) = 0, \quad (2.13)$$

Equation 2.13 relates the electrical potential to the pressure and concentration gradient present at (quasi)steady state. A null divergence for the total flux can describe different physical conditions. These conditions are described in the next subsection.

2.5.1 Null divergence of the total flux vector

There exist at least three different conditions where the divergence of \bar{j}_t is, intuitively, equal to zero. Which of these conditions is the actual one at the time of measurement has a major impact on the interpretation and calculations presented in the following chapters.

In Condition 1, the total flux vector components entering any arbitrary control volume are equal to those of the total flux vector leaving, and the same amount of material that enters the volume is the same amount that leaves it at the same time. Keeping in mind that the total flux vector describes the net amount of charge crossing a unit surface per unit time, we can observe that the amount of charge entering and leaving the volume is the same. However, this implies that there has to be a supply or removal of ions from the system at the boundaries for this condition to be physically possible. Because this is not the case under the assumption made that no external sources exist, Condition 1 contradicts not only the assumption above, but also the assumption that \bar{j}_t has a zero divergence in all the domain, including the boundaries. Without an external supply, the charges migrating away would induce a change in the electric potential gradient to compensate for the separation of charges. Hence, Condition 1 can be discarded.

Condition 2, in which the total flux runs in a closed loop, would indeed reach a divergence of zero. However, a flux in a closed loop is unlikely, not only in a laboratory setting but also in the borehole.

Finally, Condition 3, in which the net total flux equals zero at steady state, not only follows all the assumptions described previously, but it can explain why in the borehole the SP log does not depend on the electrical conductivity of rock beds and borehole mud. If Condition 3 is correct, then Equation 2.13 can be modified to describe the time-independent situation as

$$\nabla^2 V = -\nabla \cdot \left(\frac{kQ_v}{\sigma\mu} \nabla P - \frac{RT}{F} \sum_{i=1}^n \frac{t_i}{z_i} \nabla \ln c_i \right), \quad (2.14)$$

where the domain of Equation 2.14 fulfills a zero total current condition in all its points. Equation 2.14 is Poisson's equation for the electric potential. The term on the right-hand side of Equation 2.14 is called the source of the electric potential, which depends on concentration and pressure gradients. It is important to remark that in Equation 2.14 a non-zero well-defined electric potential field can exist without any external (artificial) power source and without having a closed circuit. For this reason, V in Equation 2.14 is also known as the open-circuit electric potential (Koryta *et al.*, 1994).

CHAPTER 3: PETROPHYSICS OF SPONTANEOUS POTENTIAL LOGS

This chapter introduces some classical concepts in SP literature, such as SP currents, sandstone and shale baselines, and the different factors that affect SP logs. This discussion summarizes the current understanding of SP logs and indicates how this work relates to previous knowledge. At the core of this chapter are models that link petrophysics to SP phenomena. These models are used in following chapters to relate SP logs to hydrocarbon pore volume.

3.1 SPONTANEOUS POTENTIAL CURRENTS

The term *SP currents* was coined in Doll (1949). Figure 3.1 shows a classical depiction of SP currents, commonly found in log interpretation charts used worldwide for the interpretation and correction of SP logs.

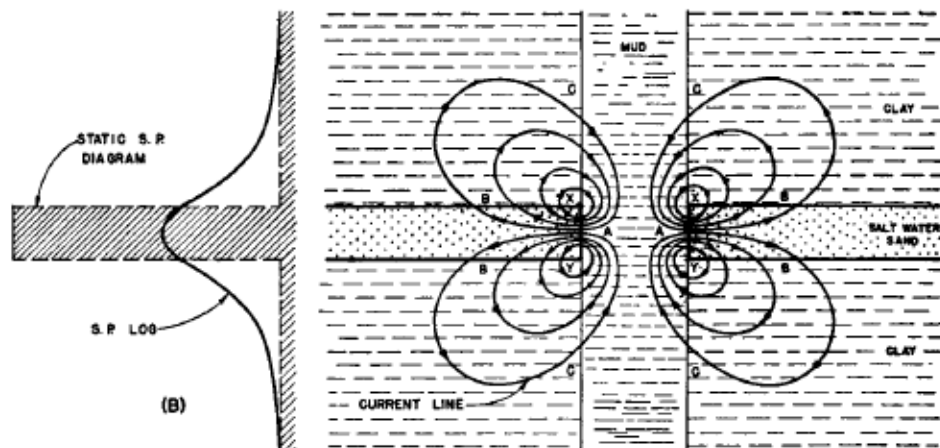


Figure 3.1: SP currents as conceived by H.G. Doll. These currents complete a closed circuit in the borehole and in the rock beds [reproduced from Doll, 1949].

However, SP currents are not based on mass transport principles but on electrical circuit principles. This results in a distorted and incorrect picture of the origin of the SP

log. The currents depicted in Figure 3.1, running from the borehole through the membrane bed all the way to the sandstone bed, are not only physically impossible, but also contradict the principles on which coupled fluxes and irreversible thermodynamics are based on (Eijkel and van den Berg, 2010). Secondly, adding a barrier to avoid SP currents (Figure 3.2) would not represent an obstacle for ions to diffuse and still produce electrical potential gradients. This is because Doll's (1949) interpretation is based on a circuit model in which, for currents to flow, the circuit must be closed. Disregarding mass transport as the origin of the SP phenomenon and ignoring the open-circuit potentials in mass diffusion disqualify the SP currents as a valid model to describe the spontaneous potential observed in the borehole.

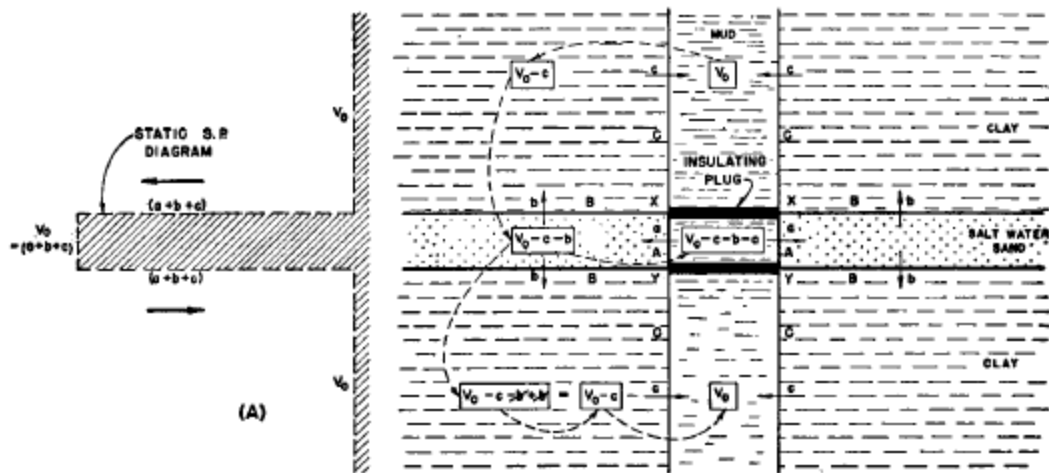


Figure 3.2: Insulating plug that opens the electrical circuit conceived by H.G. Doll, and which, in theory, would not allow the flow of SP currents [reproduced from Doll, 1949].

The rest of this chapter introduces different petrophysical models that connect the equations presented in Chapter 2 to all the petrophysical properties of interest in this project, such as hydrocarbon saturation, porosity, or formation water resistivity.

3.2 DEPENDENCE OF SPONTANEOUS POTENTIAL ON CONDUCTIVITY

Equation 2.14 states that the current source that results from pressure gradients depends on electrical conductivity. However, contrary to prior research on electrical conductivity dependence (Doll, 1949; Glowinski *et al.*, 1988; Tatsien *et al.*, 1994), the source from concentration gradients is independent of any electrical conductivity factor. This is not the case for the electrokinetic potential component, given that electrical conductivity remains present in Equation 2.14 during steady-state flow. Both the dependence and independence from electrical conductivity for both types of SP phenomena can be and were verified in laboratory experiments (Ahmad, 1964; Allègre *et al.*, 2010; Hill and Anderson, 1959; Vasconcelos *et al.*, 2014) and from field data analyzed by the author.

In the borehole, in most cases the electrochemical component of spontaneous potentials is dominant over that of the electrokinetic component (Doll, 1950; Hill and Anderson, 1959; Mounce and Rust, 1944). It is of utmost importance to interpret SP logs without any resistivity correction, as these corrections are not necessary and would lead to erroneous results if, for example, formation water salinity is calculated from SP measurements. Other corrections, however, are still necessary. The following section introduces the most common factors that affect the SP log in the borehole.

3.3 FACTORS AFFECTING SPONTANEOUS POTENTIAL LOGS

From Equation 2.14, different properties such as electrical conductivity, ion valence, or pressure and concentration gradients have a direct impact on the electric potential. However, less obvious are other properties such as bed thickness, net-to-gross ratio, clay content or hydrocarbon content, which will have, as evidenced in the field, a direct impact on SP measurements. Table 3.1 lists the most common properties that alter

the amplitude and shape of SP logs, including petrophysical properties such as porosity and water saturation.

Petrophysical properties	Water saturation
	Pore-size distribution
	Clay content
	Water salinity
	Porosity
	Irreducible water saturation
	Rock mineralogy
Geometrical properties	Borehole size
	Bed thickness
	Net-to-gross ratio
	Invasion radius
	Dip/deviation

Table 3.1: Properties that affect the SP log in a borehole.

While the geometrical factors are taken into account when Poisson's equation is solved, the petrophysical properties in Table 3.1 do not seem to be related to Equation 2.14. Nevertheless, transport numbers, electrical conductivity, permeability or charge density are all related to the petrophysical properties listed in Table 3.1. Hence, a model is necessary to relate the petrophysical properties of a rock and the way ions move through it, similar to the need for equations of state for thermodynamic problems. If this model can become a one-to-one function with water saturation, having other parameters fixed, then the quantification of hydrocarbon pore volume from SP logs would be feasible.

3.4 MEASURING SP IN THE BOREHOLE

Figure 3.3 shows how an SP log is acquired. The log is based on the potential difference between two electrodes, one grounded on the surface and the other moving along the borehole.

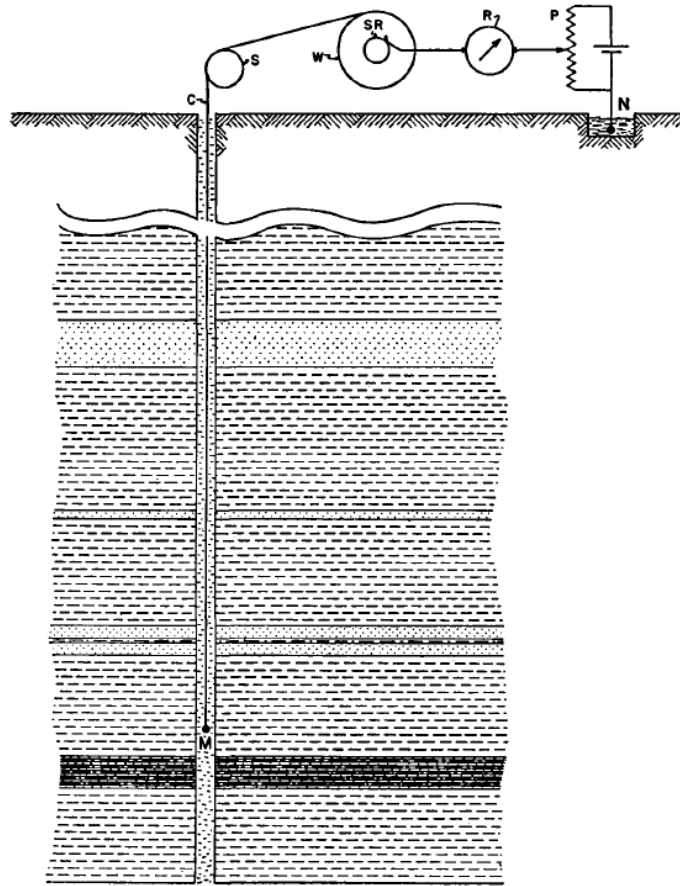


Figure 3.3: Illustration of the basic SP equipment. Electrode N is the reference electrode, while electrode M is the moving electrode in the borehole. Differences of electric potential between these electrodes are the basis of the conventional SP log [reproduced from Doll, 1949].

Although SP logs are commonly compared to an electrochemical battery, the SP log and the battery are different. Furthermore, a comparison of the SP log with a chamber

(or two) divided by a membrane, just as in the example described in Chapter 2, is widely used to explain the different potential components. However, as clearly pointed out by Mounce and Rust (1944), the SP log only measures differences of electric potential between an electrode in the surface and one in the borehole, both being in the same fluid and having no membrane between them (Figure 3.3).

The SP log measures the different electric potentials developed in front of each rock bed, resulting from the movement of ions as described by Equation 2.14. However, the values that result in a sandstone bed, for example, correspond to the addition of the liquid-junction potential and the membrane potential from the shale shoulder bed, which is why the SP is compared to an electrochemical cell. The simulator introduced in Chapter 4 shows clearly that Equation 2.14 can be solved numerically for a simple case, revealing that the result is equivalent to that obtained from adding the electric potential differences from Equations 2.4 and 2.6.

3.4.1 Sandstone and shale baselines

The classical interpretation of SP logs depends heavily on the identification of two important components: the sandstone and the shale baselines. These values correspond to the SP measured in front of a thick and clean sandstone (or any other lithology, as long as it is clay-free) and that measured in front of a thick and clean shale, respectively. Figure 3.4 is a schematic of both baselines. Because the SP log is a measurement without a natural absolute zero value, the value at shale beds is usually taken as the relative zero of the SP log. Any negative deflection from the shale baseline is interpreted as a permeable rock that bears water saltier than the mud in the borehole; a positive deflection indicates the opposite case.

Interpretations performed in the last decades assume that shales are perfect semi-permeable membranes, meaning that they only allow the passage of counterions through their pores, impeding or restricting severely the movement of anions through them. Although shales are mostly regarded as good semi-permeable membranes (Al-Bazali *et al.*, 2005; Dickey, 1944; Hill and Milburn, 1956; Lomba *et al.*, 2000; Woodruff *et al.*, 2010), differences in their permeability to anions can produce shifts in the shale baseline, introducing uncertainty in the calculations, notably when information about shale permeability to ions and presence of fractures is not available.

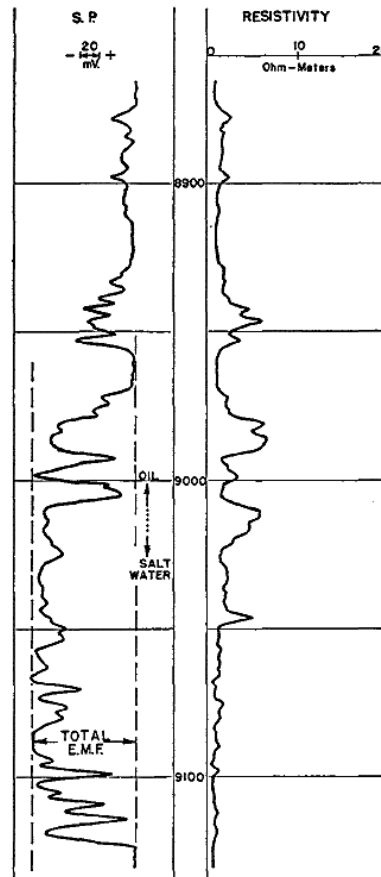


Figure 3.4: Shale (right) and sandstone (left) baselines as dashed lines on the first track [reproduced from Doll, 1949].

Figure 3.5 is a good example of shale baseline shifting. Apart from shale permeability, presence of intercalated shale in thin layers, or of non-shale and shale layers, can have a noticeable effect on the effective transport number of the rock bed, even when shale layers are perfect semi-permeable membranes. Examples of this can be found in Chapter 5.

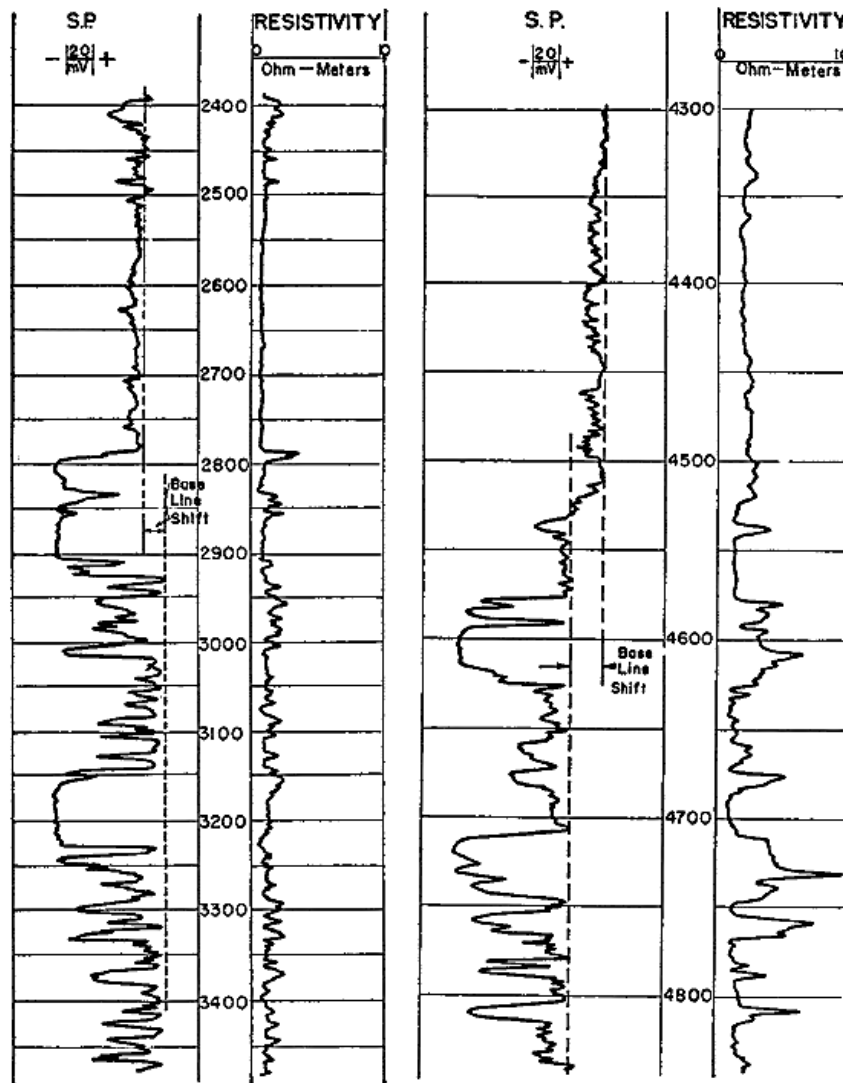


Figure 3.5: Shale baseline shifting in two field examples [reproduced from Doll, 1949].

3.5 GEOMETRICAL ASPECTS

Recognized since early publications (Doll, 1949; Segesman, 1962; Segesman and Tixier, 1959), the SP curve can be significantly affected by different geometrical properties, such as borehole size, rock bed thickness, and radius of invasion. Figure 3.6, based on SP numerical simulations on synthetic models of vertical wells with horizontal beds, shows how the normalized SP is a function of normalized bed thickness, all other properties remaining constant. In Figure 3.6, the plot resembles a saturation curve, a value of 100% corresponding to the maximum SP deflection possible in front of a thick porous bed rock. In practice, these types of rock beds are useful in determining the true SP deflection due to electrochemical origin, usually assuming that the electrokinetic component is negligible (Doll, 1949; Leinov and Jackson, 2014; Mounce and Rust, 1944; Saunders *et al.*, 2006). Figure 3.6 is independent of temperature or electrical conductivity.

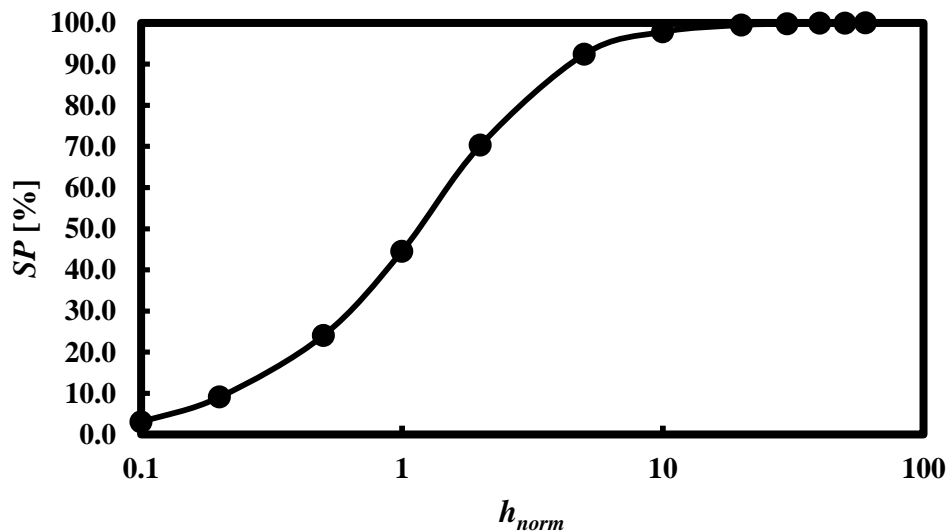


Figure 3.6: Normalized SP as a function of normalized thickness. A 100% SP indicates that the maximum SP is attained across the rock bed for any given salinity ratio and temperature.

For a conventional borehole of 8.5 inches (0.708 ft), horizontal beds thicker than 7 ft develop a full SP deflection when no mud-filtrate invasion occurs. Normalized thickness in Figure 3.6 is defined as

$$h_{norm} = \frac{h}{r_{bh} + r_{inv}}, \quad (3.1)$$

where h is bed thickness, r_{bh} is borehole radius, r_{inv} is invasion radius, and h_{norm} is normalized thickness. Mud-filtrate invasion, assuming a piston-like front, can noticeably reduce the deflection in thin beds. Nonetheless, in the case of thick beds, invasion has negligible effects, reducing the SP potential only below a normalized thickness of 10. Examples of this behavior are described in Chapter 5.

Dip, contrary to invasion or rock bed thickness, is not discussed in any work on SP, as the common assumption is that of a vertical well with horizontal layers. Only the work of Dakhnov (1962) considers analytically the behavior of SP when dip is present. Figure 3.7 shows the effect that dip has for two layers with different thickness.

To generate Figure 3.7, the shale beds are assumed to be perfect semi-permeable membranes, the salinity of the borehole mud and of the formation water are 5,000 and 25,000 ppm, respectively, containing only NaCl. The temperature for the model is 125 °F. The size of the pores in the permeable reservoir is assumed to be much larger than the EDL thickness, so any surface effect in the SP log is insignificant. Only the electrochemical component of the SP log is shown in Figure 3.7 because the electrokinetic component is assumed to be negligible. All rock beds are water-bearing only. The borehole diameter is 8.5 inches and the SP log simulations assume no mud-filtrate invasion.

An important concept to bear in mind when dealing with dipping beds with respect to the borehole axis is that, while the surface in contact with the borehole increases, this

does not necessarily result in an increase in the SP signal because the borehole is no longer symmetric. Although strictly asymmetric, the borehole may appear symmetric along a definite thickness if observed near the borehole. This thickness where apparent symmetry exists is the “effective dipping thickness.” The relationship between dip, true thickness and effective thickness of a dipping layer is given as

$$h_{eff,dip} = \frac{h}{\cos(\theta_{dip})} - 2r_{bh} \tan(\theta_{dip}), \quad (3.2)$$

where θ_{dip} is dip and $h_{eff,dip}$ is effective dip thickness based on the dip of the bed. Using Figure 3.1, $h_{eff,dip}$ is the thickness that needs to be normalized by the invasion and borehole radii in Equation 3.1.

An important consequence from Equation 3.2 is that when the first term is smaller than the second one, on the right-hand side of the equation, for a given dip, the bed becomes “invisible” for the SP because the borehole is larger than the bed itself. However, if the first term grows faster than the second one, beds whose thickness might not be enough to be observed when zero relative dip exists would become visible with dip present. In practical terms, this behavior opens the possibility of identifying beds in deviated wells or beds dipping with better vertical resolution. Figure 3.8 shows how dip changes the effective thickness for different beds for two different borehole radii, which ultimately impacts the maximum SP that can be developed in practice.

3.6 PETROPHYSICAL THEORY OF SP

Figure 3.9 shows a bundle of capillary tubes with a thin dark blue region representing the zone where the EDL has locally altered the neutral concentration of ions.

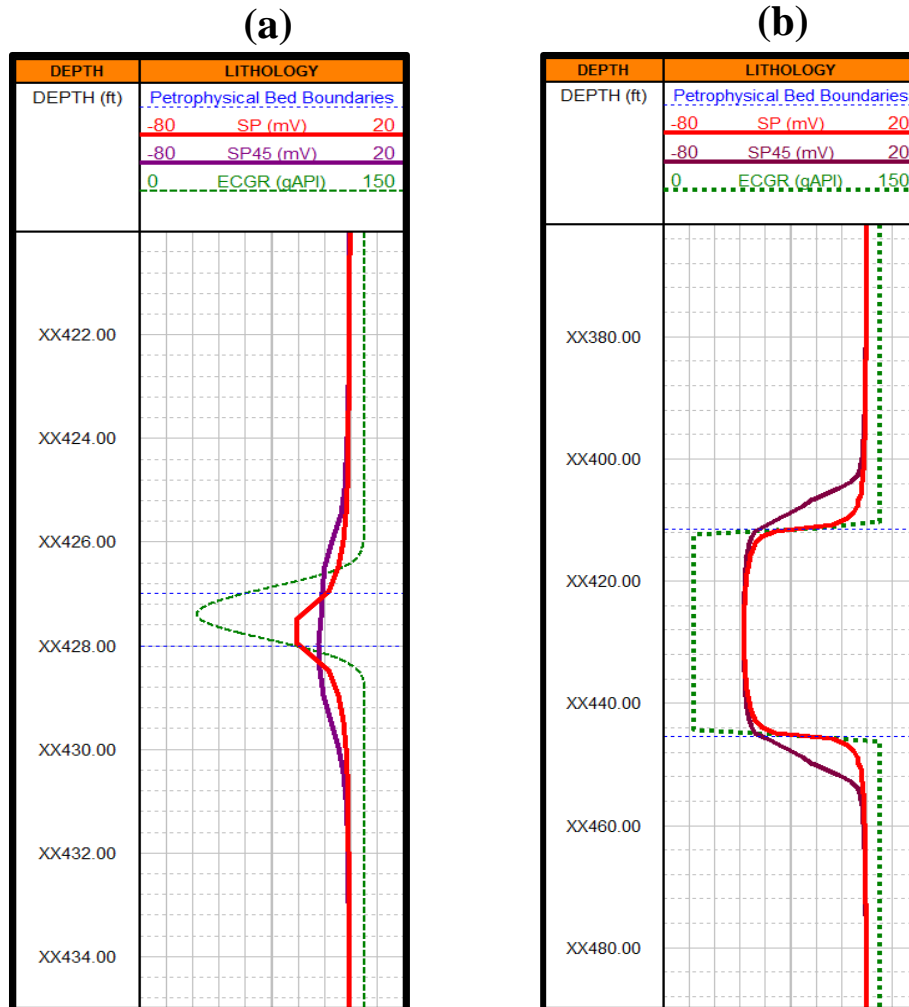


Figure 3.7: Effect of dip on SP logs for a thin and a thick bed for a dip of 0 and 45 degrees for a 3-layered synthetic model. In Track (a) the SP amplitude is smaller than in track (b), corresponding to their effective dip thickness. The logs present in tracks (a) and (b) are: gamma-ray (green, dashed), SP for horizontal beds (red), and SP for dipping beds (purple). Bed boundaries are shown as blue dashed horizontal lines.

Based on this model of porous media, the sections below elaborate on each kind of SP source (electrochemical or electrokinetic) individually from a petrophysical perspective.

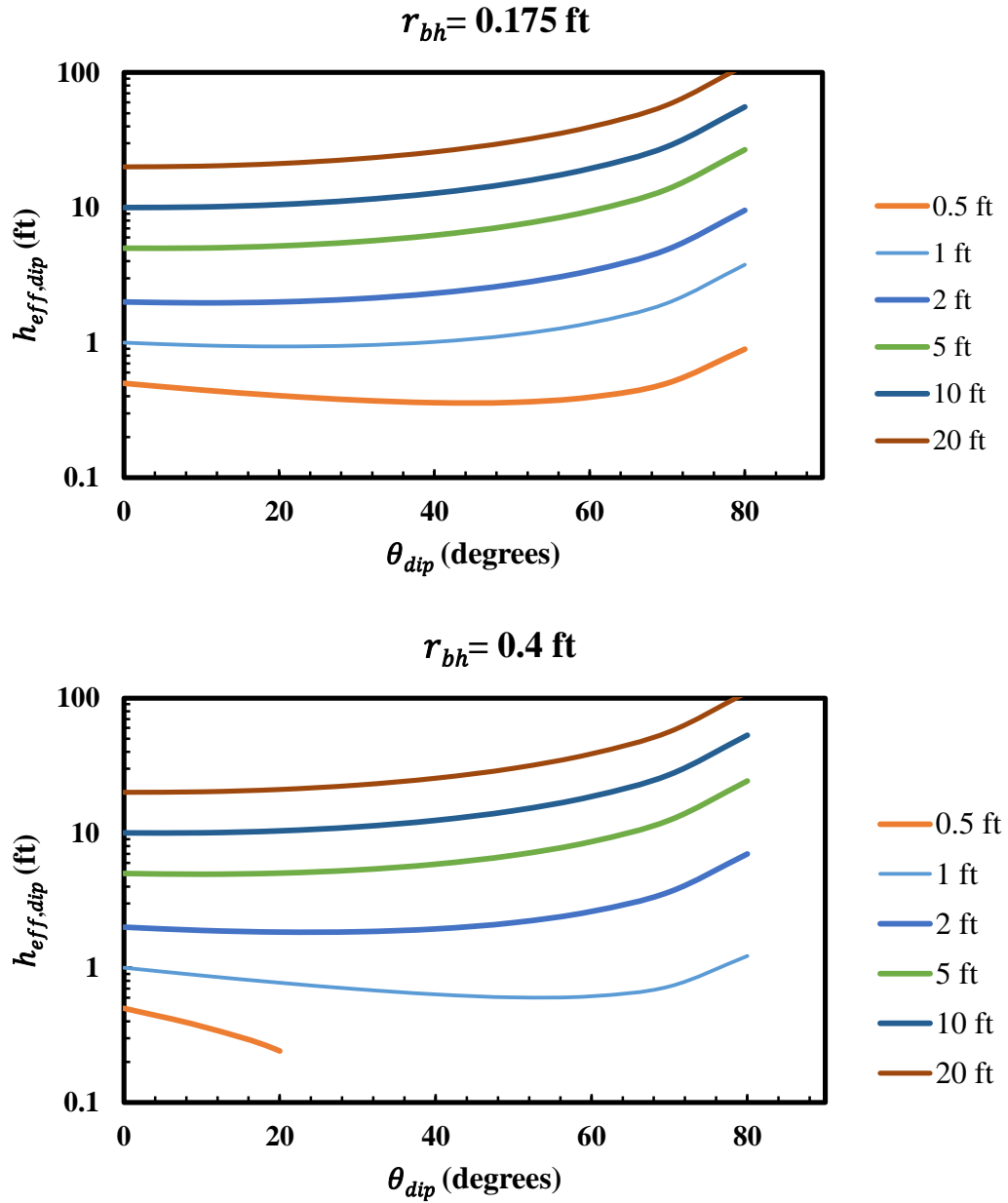


Figure 3.8: Effective dip thickness for beds of different thickness and dip in different boreholes, following Equation 3.2.

3.6.1 Electrochemical source under a petrophysical perspective

The properties that relate mass transport of ions with petrophysical properties of rocks are the ion concentration and the transport numbers of each ion. Regarding ion concentration, measurements can be made under the assumption that concentration is uniform, except at the electrical double layer. Transport numbers can be related to water saturation, porosity, or irreducible water saturation by the way diffusion of each ion is hindered or enhanced through the pore volume.

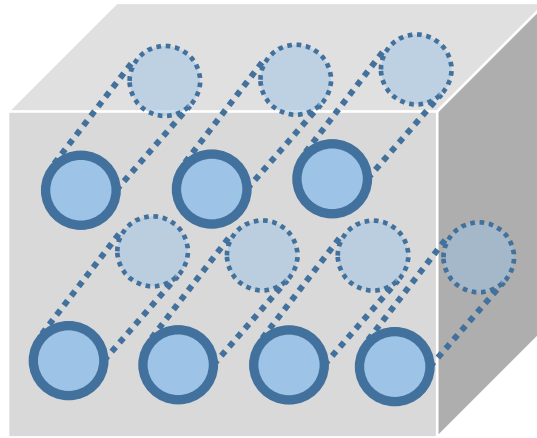


Figure 3.9: Bundle of capillary tubes for a representative elementary volume. These tubes are independent of each other, not crossing or communicating among themselves. The dark blue region corresponds to the EDL zone (not to scale), while the clear blue region is the bulk region, where bulk solution properties dominate.

In an electrolyte where no porous media exist, D_i is unique and does not change with position, assuming that the concentration of ion i is uniform. However, with a porous medium containing the electrolyte, the diffusion of ion i will tend to be hindered by the tortuosity of the pore network (Gimmi and Kosakowski, 2011; Kärger and Valiullin, 2011). A model based on a volumetric averaging for mass diffusion,

$$D_{i,eff} = v_{bulk}D_{i,bulk} + v_{EDL}D_{i,EDL} + v_{clay}D_{i,clay}, \quad (3.3)$$

calculates the effective diffusivity for each particular ion, if the diffusivity of that ion is known in each of the regions (Kärger and Valiullin, 2011; Stallmach and Kärger, 1999), as well as their volume fractions in the rock. Each volume fraction (v_j) represents the fraction of the porous space where the ion has a particular diffusivity constant. For rocks with a laminated topology of clay (i.e., laminated sands),

$$D_{i,eff} = (1 - Q_{vn})(S_{w,free}D_{i,bulk} + S_{w,EDL}D_{i,EDL}) + Q_{vn}D_{i,clay}, \quad (3.4)$$

where Q_{vn} represents the fraction of the porous space that is porous space of shale/clay (Juhász, 1981), and $S_{w,k}$ is water saturation in region k of the pore network. For a laminated or a dispersed-clay topology, the definition in Equation 3.4 remains valid, as Q_{vn} does not need to change based on the topology of the shale component.

Equation 3.4 relates the transport number of each ion with the water free of EDL available, $S_{w,free}$. In water-wet porous media, as $S_{w,free}$ decreases because of the introduction of hydrocarbons in the pore space, the value of $D_{i,eff}$ varies accordingly, resulting in a different value of transport number and, in turn, yielding a different SP voltage. Equation 3.4 can be applied in cases where rocks are clay free and where only the EDL from quartz or calcite grains affects the overall diffusion constant of each ion. Thus, discussions and models (Coates and Miller, 1998; Hill and Milburn, 1956; Ortiz *et al.*, 1972; Woodruff *et al.*, 2010) in which clay is deemed necessary to detect the presence of hydrocarbons in SP logs, are only partially correct.

Two key parameters introduced with Equation 3.4 are $D_{i,EDL}$ and $S_{w,EDL}$. Both of these parameters depend on the rock pore-size distribution, as well as on the thickness of the EDL. Taking the model of a capillary tube, it can be shown that

$$S_{w,EDL} = \frac{S}{V_p} \lambda = \left[\frac{2(1 - \phi)}{\phi} \sum_{j=1}^m \frac{f_j}{r_j} \right] \lambda, \quad (3.5)$$

where S is surface area of mineral grains, V_p is pore volume, ϕ is porosity, f_j is fraction of capillary tubes with radius r_j , and λ is EDL thickness. Equation 3.5 provides a link between SP and porosity. However, given the small value of λ (no more than a few hundreds of nanometers), one can expect porosity to have a small effect on SP logs. The only exception to this conclusion is rocks with very low porosity or with a pore-size distribution skewed toward the nanoscale region. Only in those cases can SP logs be expected to be porosity dependent. Otherwise, SP logs can be treated independent of porosity (Doll, 1949).

Another key parameter in actual porous media is tortuosity, which cannot be captured in the modeling of a bundle of straight tubes. However, the effect tortuosity has on $S_{w,EDL}$ is negligible because it affects both S and V_p , cancelling its effect at the moment of taking the quotient shown in Equation 3.5. This is not the case for the values of diffusivity in Equation 3.4, which are known to scale with tortuosity (Revil and Jougnot, 2008) as

$$D = \frac{D_o \phi}{\tau}, \quad (3.6)$$

where D is diffusion coefficient, D_o is diffusion coefficient in water without porous media, and τ is tortuosity.

Diffusivity values for ions in the EDL are conventionally not available, as most measurements of diffusivity in porous media attempt only to obtain effective diffusivity. In order to obtain the values in the region of the double layer, it is proposed that high-field NMR methods can yield these values for certain ions such as chlorine, sodium or potassium. Measurements of diffusivity values are not available yet, thus arbitrary physically feasible values are used in the rest of this work.

Figure 3.10 shows the effect that water saturation has on normalized SP, particularly when diffusivity on the EDL for cations exceeds by a factor of 10 the diffusivity in the bulk solution. In this figure, it was assumed that the electrolyte contains only Na and Cl ions. With Figure 3.10 it is possible to explain laboratory observations (McCall *et al.*, 1971; Ortiz *et al.*, 1972), where the SP across a rock becomes a function of water saturation, leading to a more shale-like electrochemical potential at low pore volume water. Although a solid confirmation is still necessary, for now it is claimed that the differences in all the experiments (McCall *et al.*, 1971; Ortiz *et al.*, 1972) are due to differences in porosity, surface chemistry, pore-size distribution, and size of the EDL. Extrapolating this to field application, it is expected that different formations will respond differently, being more or less sensitive to changes in water saturation depending on their surface chemistry. In Figure 3.10 (b), a one-to-one relationship can be built between water saturation and SP voltage, while in (a), in the same figure, the narrow interval of values in which the SP varies can make the estimations of water saturation from SP logs unreliable and highly uncertain, except at low water saturation (i.e., $S_w < 0.3$). This observation is reported in several works (Kerver and Prokop, 1957; McCall *et al.*, 1971; Ortiz *et al.*, 1972).

Shales and clay-free rocks can yield the same SP response. The pore-size distribution and high charge density of shales favor the diffusion of cations over that of

anions. This behavior results in transport numbers of cations being near or equal to 1, resulting in a semi-permeable membrane potential. Clay-free rocks can also develop membrane-like potentials if their pore throats are small enough to hinder the movement of ions by the EDL. If this is not the case, then a conventional liquid-junction potential is developed. A good example of the relationship between throat-size distribution and SP can be found in McCall *et al.* (1971), whose particular figure of interest is reproduced as Figure 3.11 in this report.

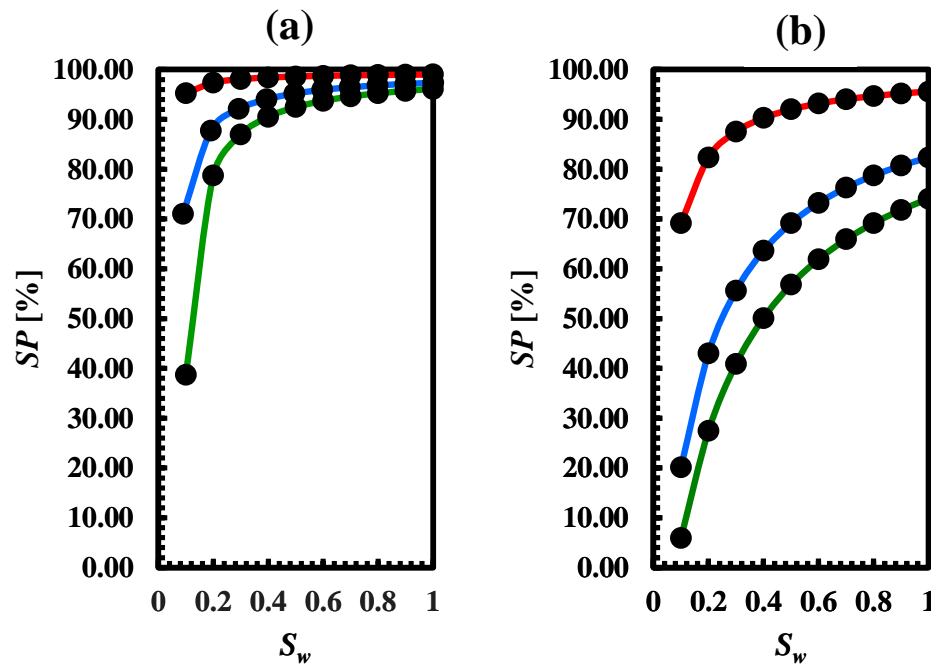


Figure 3.10: Effect of water saturation on the normalized SP for different values of $S_{w,EDL}$: 0.01 (red), 0.05 (blue), and 0.08 (green). In (a) there is no diffusivity improvement for cations in the EDL. In (b) the diffusivity of cations in the EDL is ten times higher than in the bulk solution (see Table 3.2).

	(a)	(b)
$D_{Na,bulk}$	$1 \times 10^{-6} \text{ cm}^2/\text{s}$	$1 \times 10^{-6} \text{ cm}^2/\text{s}$
$D_{Cl,bulk}$	$1.54 \times 10^{-6} \text{ cm}^2/\text{s}$	$1.54 \times 10^{-6} \text{ cm}^2/\text{s}$
$D_{Na,EDL}$	$1 \times 10^{-6} \text{ cm}^2/\text{s}$	$1 \times 10^{-5} \text{ cm}^2/\text{s}$
$D_{Cl,EDL}$	$1 \times 10^{-8} \text{ cm}^2/\text{s}$	$1 \times 10^{-8} \text{ cm}^2/\text{s}$

Table 3.2: Values used for generating Figure 3.10.

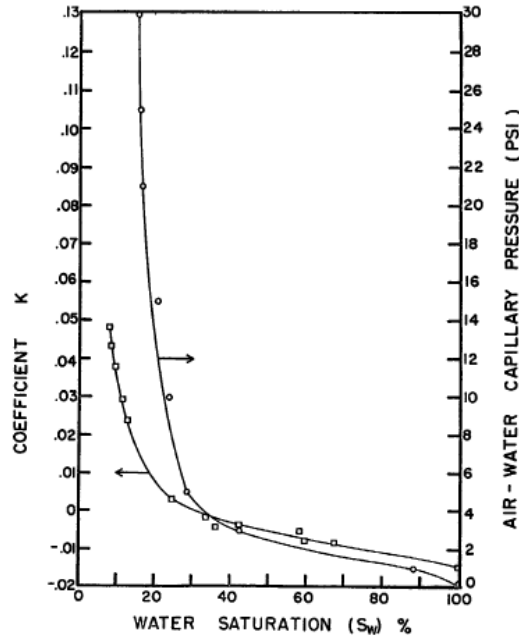


Figure 3.11: SP coefficient [$K = RF^{-1}(t_{Na} - t_{Cl})$] and capillary pressure as a function of water saturation. In both curves, a decrease in the water saturation corresponds to an increase in both capillary pressure and SP magnitude [reproduced from McCall et al. (1971)].

3.6.2 Electrokinetic source under a petrophysical perspective

The electrokinetic source appears from the displacement of cations near the fluid-matrix interface (Ahmad, 1964; Bolève *et al.*, 2007; Darnet and Marquis, 2004; Hill and Anderson, 1959) due to viscous dragging from the water being displaced. As the fluids are

displaced downstream, extra cations accumulate until the electric potential gradient is large enough to make them flow against the bulk flow direction to compensate for the abnormal charge accumulation.

The main petrophysical properties in the electrokinetic source are permeability and Q_v , the charge density in the pore space. From Revil (1999), it is known that Q_v depends on the cation-exchange capacity (CEC) of the matrix and its density (ρ_{dry}), following

$$Q_v = CEC \rho_{dry} \frac{1 - \phi}{\phi}. \quad (3.7)$$

Shales possess a relatively high CEC, which in turn, provides them with high values of Q_v . In contrast, quartz or calcite has relatively low values of CEC. The values of CEC can be changed by pH, temperature and electrolyte concentration or composition, as this alters the surface chemistry of the rock (Revil *et al.*, 1998; Revil and Leroy, 2004). Another option to increase or decrease the CEC is by modifying the specific surface of the matrix. That is the main reason why shales, with higher specific surface than calcite or quartz, have a higher CEC (Revil and Leroy, 2004).

In most cases with brine-saturated reservoirs, the electrokinetic component can be expected to be negligible, particularly if mudcake is formed by the time the measurements are acquired, thereby yielding a similar streaming potential in front of shale and non-shale beds.

CHAPTER 4: SIMULATION CODE

Chapter 4 describes the discretized grid and equations used in the finite-difference algorithm written for the numerical simulation of SP logs. Additionally, this chapter presents equations to approximate properties at gridblock boundaries, as well as boundary conditions used in SP log numerical simulations. The chapter concludes by showing how the system of equations that results from discretizing Equation 2.14 is solved by the bi-conjugate gradient method and why this method is preferred over other methods to solve for the SP log in the borehole.

4.1 DISCRETE EQUATIONS

To develop the SP log simulator, Equation 2.14 is discretized in cylindrical coordinates, which are the ones that conform to the wellbore geometry. Based on Strikwerda (2004),

$$\frac{1}{r} \frac{\partial}{\partial r} \left(r \frac{\partial V}{\partial r} \right) \approx \frac{1}{r_i} \frac{1}{\Delta r_i} \left[r_{i+\frac{1}{2}} \frac{V_{i+1,j,k} - V_{i,j,k}}{\Delta r_i^+} - r_{i-\frac{1}{2}} \frac{V_{i,j,k} - V_{i-1,j,k}}{\Delta r_i^-} \right], \quad (4.1)$$

$$\frac{1}{r^2} \frac{\partial^2 V}{\partial \theta^2} \approx \frac{1}{r_i^2} \frac{1}{\Delta \theta_j^2} (V_{i,j+1,k} - 2V_{i,j,k} + V_{i,j-1,k}), \quad (4.2)$$

$$\frac{\partial^2 V}{\partial z^2} \approx \frac{1}{\Delta z_k^2} (V_{i,j,k+1} - 2V_{i,j,k} + V_{i,j,k-1}), \quad (4.3)$$

$$\frac{1}{r} \frac{\partial}{\partial r} \left(r \frac{kQ_v}{\sigma\mu} \frac{\partial P}{\partial r} \right) \approx \frac{1}{r_i} \frac{1}{\Delta r_i} \left[r_{i+\frac{1}{2}} \left(\frac{kQ_v}{\sigma\mu} \right)_{i+\frac{1}{2}} \frac{P_{i+1,j,k} - P_{i,j,k}}{\Delta r_i^+} - r_{i-\frac{1}{2}} \left(\frac{kQ_v}{\sigma\mu} \right)_{i-\frac{1}{2}} \frac{P_{i,j,k} - P_{i-1,j,k}}{\Delta r_i^-} \right], \quad (4.4)$$

$$\frac{1}{r^2} \frac{\partial}{\partial \theta} \left(\frac{kQ_v}{\sigma\mu} \frac{\partial P}{\partial \theta} \right) \approx \frac{1}{r_i^2} \frac{1}{\Delta\theta_j^2} \left[\left(\frac{kQ_v}{\sigma\mu} \right)_{j+\frac{1}{2}} (P_{i,j+1,k} - P_{i,j,k}) - \left(\frac{kQ_v}{\sigma\mu} \right)_{j-\frac{1}{2}} (P_{i,j,k} - P_{i,j-1,k}) \right], \quad (4.5)$$

$$\frac{\partial}{\partial z} \left(\frac{kQ_v}{\sigma\mu} \frac{\partial P}{\partial z} \right) \approx \frac{1}{\Delta z_k^2} \left[\left(\frac{kQ_v}{\sigma\mu} \right)_{k+\frac{1}{2}} (P_{i,j,k+1} - P_{i,j,k}) - \left(\frac{kQ_v}{\sigma\mu} \right)_{k-\frac{1}{2}} (P_{i,j,k} - P_{i,j,k-1}) \right], \quad (4.6)$$

$$\frac{RT}{F} \frac{1}{r} \frac{\partial}{\partial r} \left(r \frac{t_m}{z_m} \frac{\partial \ln c_m}{\partial r} \right) \approx \frac{RT}{F z_m} \frac{1}{r_i} \frac{1}{\Delta r_i} \left[r_{i+\frac{1}{2}} (t_m)_{i+\frac{1}{2}} \frac{\ln \frac{c_{i+1,j,k}}{c_{i,j,k}}}{\Delta r_i^+} - r_{i-\frac{1}{2}} (t_m)_{i-\frac{1}{2}} \frac{\ln \frac{c_{i,j,k}}{c_{i-1,j,k}}}{\Delta r_i^-} \right], \quad (4.7)$$

$$\frac{RT}{F} \frac{1}{r^2} \frac{\partial}{\partial \theta} \left(\frac{t_m}{z_m} \frac{\partial \ln c_m}{\partial \theta} \right) \approx \frac{RT}{F z_m} \frac{1}{r_i^2} \frac{1}{\Delta\theta_j^2} \left[(t_m)_{j+\frac{1}{2}} \left(\ln \frac{c_{i,j+1,k}}{c_{i,j,k}} \right) - (t_m)_{j-\frac{1}{2}} \left(\ln \frac{c_{i,j,k}}{c_{i,j-1,k}} \right) \right], \quad (4.8)$$

$$\frac{RT}{F} \frac{\partial}{\partial z} \left(\frac{t_m}{z_m} \frac{\partial \ln c_m}{\partial z} \right) \approx \frac{RT}{F z_m} \frac{1}{\Delta z_k^2} \left[(t_m)_{k+\frac{1}{2}} \left(\ln \frac{c_{i,j,k+1}}{c_{i,j,k}} \right) - (t_m)_{k-\frac{1}{2}} \left(\ln \frac{c_{i,j,k}}{c_{i,j,k-1}} \right) \right], \quad (4.9)$$

where Equations 4.1 through 4.9 are the discretized version of Equation 2.14 for a 3-dimensional space. Equations 4.7 through 4.9 need to be implemented for each ionic component m , given that the values at the grid boundaries need to be calculated individually for each ion and then added to yield the electrochemical source.

4.1.1 Interblock properties

The discretization given in the previous section demands that certain properties such as electrical conductivity or transport numbers be computed at gridblock boundaries, although these properties are only assigned *a priori* at grid points. To that end, based on the continuity of mass or current flux, the interblock properties are calculated as:

$$\sigma_{i+\frac{1}{2}} = (\Delta r_i + \Delta r_{i+1}) \left(\frac{\Delta r_{i+1}}{\sigma_{i+1}} + \frac{\Delta r_i}{\sigma_i} \right)^{-1}, \quad (4.10)$$

$$k_{i+\frac{1}{2}} = (\Delta r_i + \Delta r_{i+1}) \left(\frac{\Delta r_{i+1}}{k_{i+1}} + \frac{\Delta r_i}{k_i} \right)^{-1}, \quad (4.11)$$

$$Q_{v,i+\frac{1}{2}} = \frac{Q_{v,i+1} + Q_{v,i}}{2}, \quad (4.12)$$

$$\mu_{i+\frac{1}{2}} = \frac{\mu_{i+1} + \mu_i}{2}, \quad (4.13)$$

$$(t_m)_{i+\frac{1}{2}} = \frac{D_{m,i+\frac{1}{2}}}{\sum_{n=1}^N D_{n,i+\frac{1}{2}}} = \frac{\left(\frac{\Delta r_{i+1}}{\Delta D_{m,i+1}} + \frac{\Delta r_i}{\Delta D_{m,i}} \right)^{-1}}{\sum_{n=1}^N \left(\frac{\Delta r_{i+1}}{\Delta D_{n,i+1}} + \frac{\Delta r_i}{\Delta D_{n,i}} \right)^{-1}}. \quad (4.14)$$

Note that in Equation 4.14, the condition that $\sum_{n=1}^N t_n = 1$ remains valid at block boundaries. Values of diffusivity used in Equation 4.14 are calculated from Equations 3.3 or 3.4.

4.1.2 Discretization in each direction

For the z - and θ - directions, the discretization is uniform, assigning the locations of the boundaries of each grid block, and placing the grid point in the middle of each block. For the r -axis, the discretization is logarithmical from the borehole wall to the boundaries of the domain; the borehole is discretized uniformly from the borehole wall to its center. The logarithmic discretization is implemented following Settari and Aziz (1972) as:

$$\alpha = \left(\frac{r_e}{r_w}\right)^{\frac{1}{N_g}}, \quad (4.15)$$

$$r_{i+1} = \alpha r_i; \quad r_1 = \frac{r_w \ln \alpha}{1 - \left(\frac{1}{\alpha}\right)}, \quad (4.16)$$

where r_w is borehole radius, r_e is radius of the outermost gridblock boundary, and N_g is number of extant grid blocks. Inside the borehole, the first grid block boundary is located at $r = 0$.

4.2 BOUNDARY CONDITIONS

In the r -direction, the boundary is set as far as possible from the borehole, in order to avoid any limited-domain effects from the boundary that can corrupt the numerical simulations. A no-flux boundary condition is imposed at the boundaries in the r -direction. Mathematically, this condition is expressed as

$$\nabla V \cdot \hat{n}_r = 0, \quad (4.17)$$

where \hat{n}_r is the vector normal to the surface of the boundary. In the z -direction, a similar boundary condition exists, such that no ionic currents flow in z -direction. Finally, in the θ -direction, continuity of total current is imposed at each gridblock boundary. Because θ is cyclic, the total current leaving the last gridblock needs to equal the current entering the first gridblock in the θ -direction.

4.3 MATRIX ENTRIES

The problem of SP log simulation can be reduced to a system of linear equations of the form $\mathbf{Ax} = \mathbf{b}$, where \mathbf{b} represents the values of the sources, \mathbf{x} is the electric potential field to be calculated, and \mathbf{A} is the discrete Laplacian operator in cylindrical coordinates.

Vector \mathbf{x} , although it can be arranged in any arbitrary manner, is ordered first by the r coordinate, then by the z coordinate, and finally by the θ coordinate. This arrangement is described in Figure 4.1. The elements can be separated in subgroups with the same z and with the same azimuth. Based on this order, the elements of \mathbf{A} are arranged as shown in Figure 4.1. The smallest submatrices in \mathbf{A} correspond to grid points with the same z and θ coordinates; middle-sized submatrices correspond to grid points with the same θ coordinate only. If n , p , and q are the number of grid points in the r -, z -, and θ -directions respectively, then the smallest submatrices in \mathbf{A} have a size of $n \times n$, the middle-sized are $np \times np$, and matrix \mathbf{A} has a total of $npq \times npq$ entries. This means that doubling the amount of grid points in any direction increases the total amount of elements in \mathbf{A} by a factor of 4, which is important in terms of computer memory and time needed to solve for \mathbf{x} .

Calculation of vector \mathbf{b} is made by applying the discrete Laplacian matrix to the concentration and pressure discrete fields in vector form, following Equations 4.4 through 4.9. The order of the elements in the concentration and pressure values must be consistent with that of the electric potential field.

4.4 ITERATIVE SOLUTION

With the system $\mathbf{Ax} = \mathbf{b}$ formed from the input data, two options are available for the solution of this system: direct or iterative methods. The most primitive direct methods attempt to calculate \mathbf{A}^{-1} , multiply this inverse matrix by \mathbf{b} , and obtain \mathbf{x} directly as the result of this multiplication. More elaborate direct methods such as LU decomposition and Gauss elimination avoid calculating directly \mathbf{A}^{-1} by manipulating \mathbf{A} and back calculating the entries of vector \mathbf{x} . These procedures, although straightforward, can be impractical in cases where \mathbf{A} contains thousands of entries, because of computer memory requirements.

Iterative methods, on the other hand, approximate \mathbf{x} via iterative cycles of steps that vary depending on the method used. In this particular case, the SP log simulator uses the bi-conjugate gradient stabilized method. This method does not require \mathbf{A} to be symmetric (Saad, 2003; Strikwerda, 2004; van der Vorst, 1992); this property offers an advantage in this particular problem where matrix \mathbf{A} is not necessarily symmetric because of the discretization expressed in Equations 4.1 through 4.9 (Settari and Aziz, 1972). Although \mathbf{A} could be stated in a symmetric form and solved by the conjugate gradient method, the SP simulator described in this work is based on the asymmetric form of \mathbf{A} . To increase the speed of solving, a preconditioner is constructed with an incomplete LU factorization of matrix \mathbf{A} .

$$\mathbf{A} = \begin{pmatrix} \left(\begin{array}{c} \vdots \\ \vdots \\ \vdots \end{array} \right) & \left(\begin{array}{c} \vdots \\ \vdots \\ \vdots \end{array} \right) & \left(\begin{array}{c} \vdots \\ \vdots \\ \vdots \end{array} \right) \\ \left(\begin{array}{c} \vdots \\ \vdots \\ \vdots \end{array} \right) & \left(\begin{array}{c} \vdots \\ \vdots \\ \vdots \end{array} \right) & \left(\begin{array}{c} \vdots \\ \vdots \\ \vdots \end{array} \right) \\ \left(\begin{array}{c} \vdots \\ \vdots \\ \vdots \end{array} \right) & \left(\begin{array}{c} \vdots \\ \vdots \\ \vdots \end{array} \right) & \left(\begin{array}{c} \vdots \\ \vdots \\ \vdots \end{array} \right) \end{pmatrix}; \mathbf{x} = \begin{pmatrix} x_{r_1, z_1, \theta_1} \\ x_{r_2, z_1, \theta_1} \\ x_{r_3, z_1, \theta_1} \\ \vdots \\ x_{r_1, z_2, \theta_1} \\ x_{r_2, z_2, \theta_1} \\ x_{r_3, z_2, \theta_1} \\ \vdots \\ x_{r_1, z_1, \theta_2} \\ x_{r_2, z_1, \theta_2} \\ x_{r_3, z_1, \theta_2} \\ \vdots \\ x_{r_{n-2}, z_p, \theta_q} \\ x_{r_{n-1}, z_p, \theta_q} \\ x_{r_{n-1}, z_p, \theta_q} \end{pmatrix}$$

Figure 4.1: Structures of matrix \mathbf{A} and vector \mathbf{x} used to simulate SP logs.

4.5 SIMULATED SP LOG

Results obtained for vector \mathbf{x} describe the electric potential in all the domains for which V was solved. To extract the SP log from the above results, following Strikwerda (2004), the electric potential at $r = 0$ is

$$V_{0,k} = \frac{1}{M} \sum_{m=1}^M V_{1,m,k} - S(0) \left(\frac{\Delta r_{1,j,k}}{2} \right)^2, \quad (4.18)$$

where $V_{0,k}$ is the electric potential at depth k and $r = 0$, $V_{1,m,k}$ is the electric potential at the first gridpoint in r at depth k and azimuth m , M is the total amount of gridpoints in the θ -direction, $S(0)$ is the value of the SP source at $r = 0$, and $\Delta r_{1,j,k}$ is the radius of the innermost circle of gridpoints in the numerical grid. Inside the borehole, $S(0)$ is equal to zero. Hence, the calculated SP log at the center of the borehole reduces to the arithmetic average of the values at different θ values and at the first gridpoints in the r -direction (shown in blue in Figure 4.2). For axisymmetric cases, all values at the first gridpoints in r -direction are the same, resulting in an SP that can be easily extracted from these gridpoints.

The advantage offered by numerical simulations is the ability to display the complete electric potential field for the assessment of SP variation that could be of interest and that may not be sensed by the SP electrode located in the middle of the borehole.

4.6 INPUT SOURCE INFORMATION

The salt concentration and pressure fields need to be calculated in advance in the reservoir to calculate the source density that gives rise to the SP log. These calculations, which include mud-filtrate invasion and salt and pressure diffusion through rock beds, are performed in UTAPWeLS, the well logging and petrophysics software developed by the Joint Industry Research Consortium for Formation Evaluation, of The University of Texas

at Austin (Malik *et al.*, 2008; Salazar and Torres-Verdín, 2009; Voss *et al.*, 2009). Based on the constructed earth model and numerical simulation results obtained with UTAPWeLS, SP logs can be simulated in a similar manner to other logs that are simulated by the software.

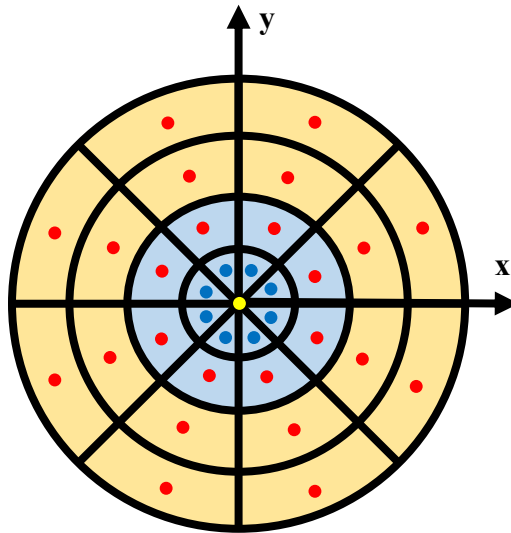


Figure 4.2: The SP log at the borehole's axis (yellow dot), at each depth, is calculated as the arithmetic average of the values of electric potential of gridpoints surrounding the origin (shown in blue) because no SP sources exist inside the borehole (see text above). The borehole is in blue and the formation is in yellow. Red dots represent the gridpoints that are not the first gridpoints in the r -direction.

4.7 ALGORITHM PERFORMANCE

Table 4.1 summarizes the CPU time and memory required to run the example shown in Figure 5.4 in Chapter 5, which is an example of a 2D SP log numerical simulation. The simulation was performed in a 64-bit desktop PC with 3.40 GHz of processing power and 32 GB of RAM memory. Chapter 5 shows more details about the algorithm's accuracy and reliability.

Number of depth point	Number of radial points	RAM Memory required	CPU Time
1,601	198	378 MB	9.24 s

Table 4.1: Summary of algorithm performance. CPU time indicates only the time necessary to obtain vector x by the bi-conjugate method. RAM memory is the total memory required for all the calculations in the algorithm.

CHAPTER 5: SYNTHETIC CASES FOR NUMERICAL SIMULATION OF SP MEASUREMENTS

This chapter documents synthetic cases for 2D and 3D measurement conditions. Results presented are focused on quantifying the effect of normalized thickness (Chapter 3), and on considering shoulder and invasion effects, thus supporting the information described in Chapters 2 through 5. Of particular interest are thin layers, specifically their impact on SP logs. Simulation of SP logs from thick, non-porous rock beds is also discussed in light of the theory presented in Chapters 2 and 3. This chapter ends showing the effect hydrocarbon pore volume has on numerically simulated SP logs. This effect is similar to that observed in the field examples described in Chapter 6.

5.1 SIMPLE SYNTHETIC CASES

A three-layered model (i.e., a sandstone bed shouldered by two shale beds at the top and at the bottom) is the most widely covered and discussed model for SP numerical simulation (Doll, 1950; Glowinski *et al.*, 1988; Salazar *et al.*, 2008; Woodruff *et al.*, 2010). Based on this model, SP has been conventionally defined as

$$SSP = K \log \left(\frac{R_w}{R_{mf}} \right) = K \log \left(\frac{C_w}{C_{mf}} \right), \quad (5.1)$$

where SSP is SP in front of a thick, clay free formation, K is a coefficient (McCall *et al.*, 1971; Woodruff *et al.*, 2010), and R_{mf} , R_w , C_{mf} , and C_w are resistivity and salinity of mud filtrate and formation water, respectively. This is the standard equation used by the petrophysical community for the estimation of water salinity/resistivity (Ellis and Singer, 2007; Woodruff *et al.*, 2010), and it assumes only the presence of NaCl in solution. Figure

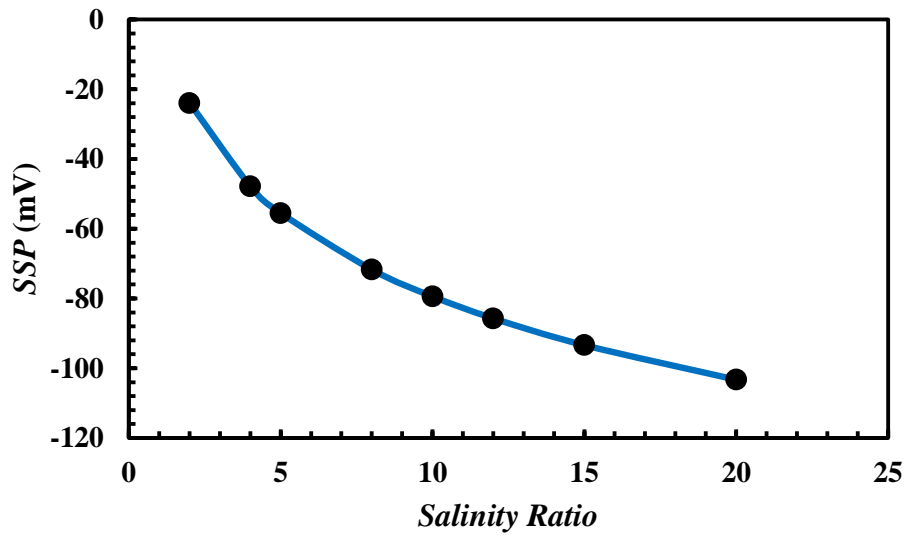


Figure 5.1: Comparison between theoretical SP values (solid line) and results from numerical simulations (dots) for a thick, clean-water-bearing horizontal rock bed penetrated by a vertical well with a 0.1 m radius. The temperature is set to 50 °C. Shale beds are assumed to be perfect semi-permeable membranes.

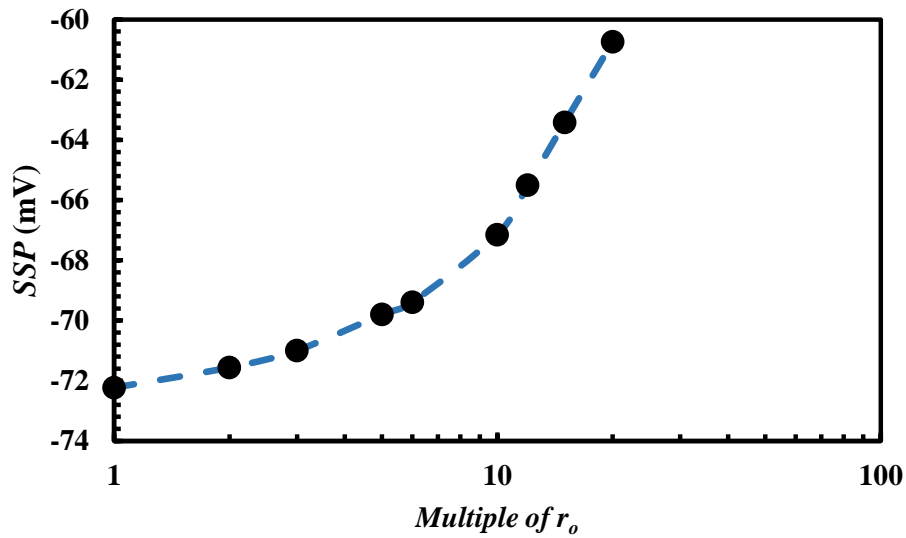


Figure 5.2: Comparison between results of increasing the original wellbore radius, r_o , of 0.1 m (dots) and mud-filtrate invading by the same length, keeping r_o unaltered (dashed line). The salinity ratio and temperature for generating this figure are 10 and 50 °C.

5.1 shows the SP log simulated at the sandstone bed with different water salinity values compared to the calculations obtained following Equation 5.1.

Figure 5.1 compares simulation results to calculations from Equation 5.1, indicating that numerical simulations are accurate in water-bearing rocks where the volume of shale/clay is negligible. The difference between numerical simulation and Equation 5.1 is on the order of 10^{-6} millivolts. However, these results assume no mud-filtrate invasion into the formation for the simulation. Figure 5.2 compares the numerically simulated SP for different invasion radii and different wellbore radii, but with no invasion. The plots confirm the comments in Doll (1949) about the equivalence of invasion or enlargement of the borehole radius.

Table 5.1 describes the case of equal salinity between the borehole and the permeable formation. The four results documented in that table assume the same properties for the permeable formation, but not for the shouldering shales, which vary in water salinity by 50, 80 and 100 kppm, and a combination of 50 and 100 kppm, yielding exactly the same SP log. All these results assume that shoulder beds are perfect semi-permeable membranes. As long as the latter assumption is correct, it is possible to neglect the salinity of the shales in SP log simulation, contrary to other measurements, such as resistivity and nuclear logs.

Salinity in shale	100 kppm	80 kppm	50 kppm	50 and 100 kppm
SP (mV)	0	0	0	0

Table 5.1: Numerical results obtained for a case in which the borehole mud and formation water exhibit the same water salinity. The result is the same, regardless of the salinity of the shale beds that shoulder the permeable bed. SP is measured as the deflection from the shale baseline. A zero SP indicates that no deflection occurs along the permeable bed.

Given that increases of invasion and borehole radii are equivalent, it is found that invasion has no effect on the SP amplitude across thick layers, unless it is a severe case of fluid loss or of gravity affecting the distribution of salt concentration (Segesman and Tixier, 1959). The practical implication of this behavior is that it is necessary to find a layer whose normalized thickness (see Chapter 3) is at least equal to 10 to make an adequate quantification of formation water salinity from the SP log across a formation without clay content.

Figure 5.3 compares the SP log that would be taken at different times from the onset of mud-filtrate invasion in the same borehole. As invasion time increases, the salt concentration front not only moves into the bed but also changes its shape, from a sharp front to a sigmoidally shaped front. This behavior is a consequence of the magnitude and spread of the salt concentration gradient and may or may not be disregarded in practical interpretation problems, depending on the case of interest.

5.1.1 Bed thickness effect

Figure 5.4 describes simulation results for rock beds with different thicknesses. Following the results from Figures 5.2 and 5.3, the beds with a normalized thickness below 10 are below the highest SP value that can be attained by a permeable bed. This effect is not, as could be inferred, a problem with numerical grid resolution. The loss of resolution is a consequence of the Poisson's equation that governs the electric potential, as given by Equation 2.14.

The Laplacian operator, from a discrete perspective, can be thought of as an operator that averages the values of the surrounding gridpoints to yield the value of the point where it is centered (Strikwerda, 2004). The Laplacian operator has this averaging property because it is linear and, thus, the principle of superposition is applicable. The

averaging commonly observed in field and numerical SP logs, especially in the case of alternating thin laminations, exists because of superposition. To illustrate this principle, two cases are compared in Figure 5.5, where smaller laminations have a more pronounced averaging than do thicker laminations due to spatial superposition of the electric potential.

Contrary to other tools with an artificial source, SP tools measure the already-distributed sources inside the rock beds. The farther from the SP sources, the more noticeable is the superposition effect on the electric potential observed. Hence, the center of the borehole is both a less than ideal position in terms of resolution and unnecessary when acquiring measurements. With a smaller borehole, the SP electrode is much closer to the sources, avoiding the decrease of vertical resolution. From a signal analysis perspective, once superposition has affected the measurements, information about individual beds is lost, and recovering it is difficult or impossible. However, for those layers that show a significant reading in the borehole, deconvolution can be applied to estimate the SP from every layer, not just from thick beds, in order to read the *SSP* correctly. This approach is currently under development by the author, and it is expected to be included in a future doctoral dissertation.

5.1.2 Thick rock beds impermeable to ions and fluids

In Figure 5.6 the center layer at the five-layered model possesses no permeability and no porosity. Without those properties, no pressure gradient and no concentration gradient exists. The practical implication of this result is that the baseline from a non-porous impermeable formation can always be assigned the value of absolute zero. With this absolute baseline, and with subsequent SP processing, it could be possible to extend SP interpretation to limestone formations, where thick formations are common and usually no shale beds exist.

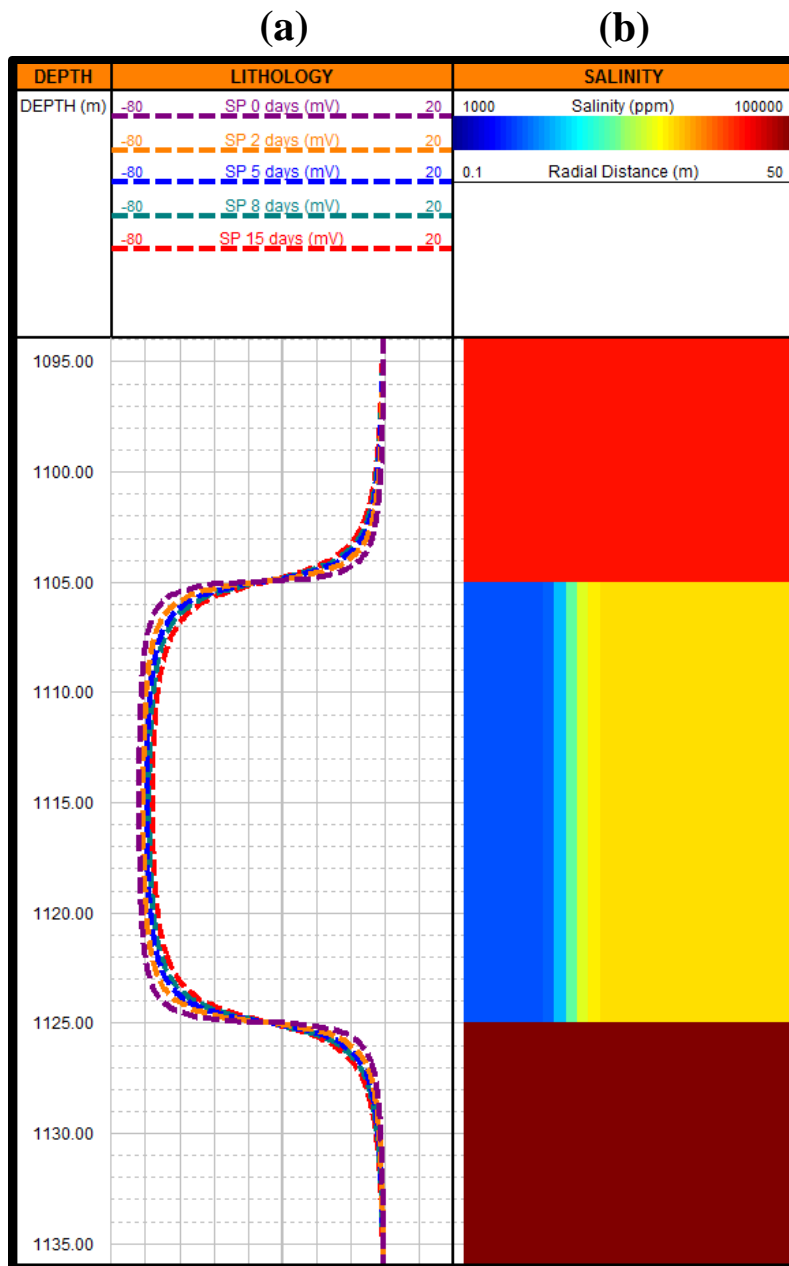


Figure 5.3: Track (a): SP log simulated on different days after the onset of mud-filtrate invasion shown on the first track. The SP simulator can take the radial distribution into account and calculate the electrochemical SP log. Shales are assumed to be perfect semi-permeable membranes. The temperature is set to 122 °F. The salinity ratio for this example is 15. The borehole has a radius of 10 cm. All layers are water-bearing. Track (b): Salt concentration profile on that corresponds to mud-filtrate invasion after 15 days.

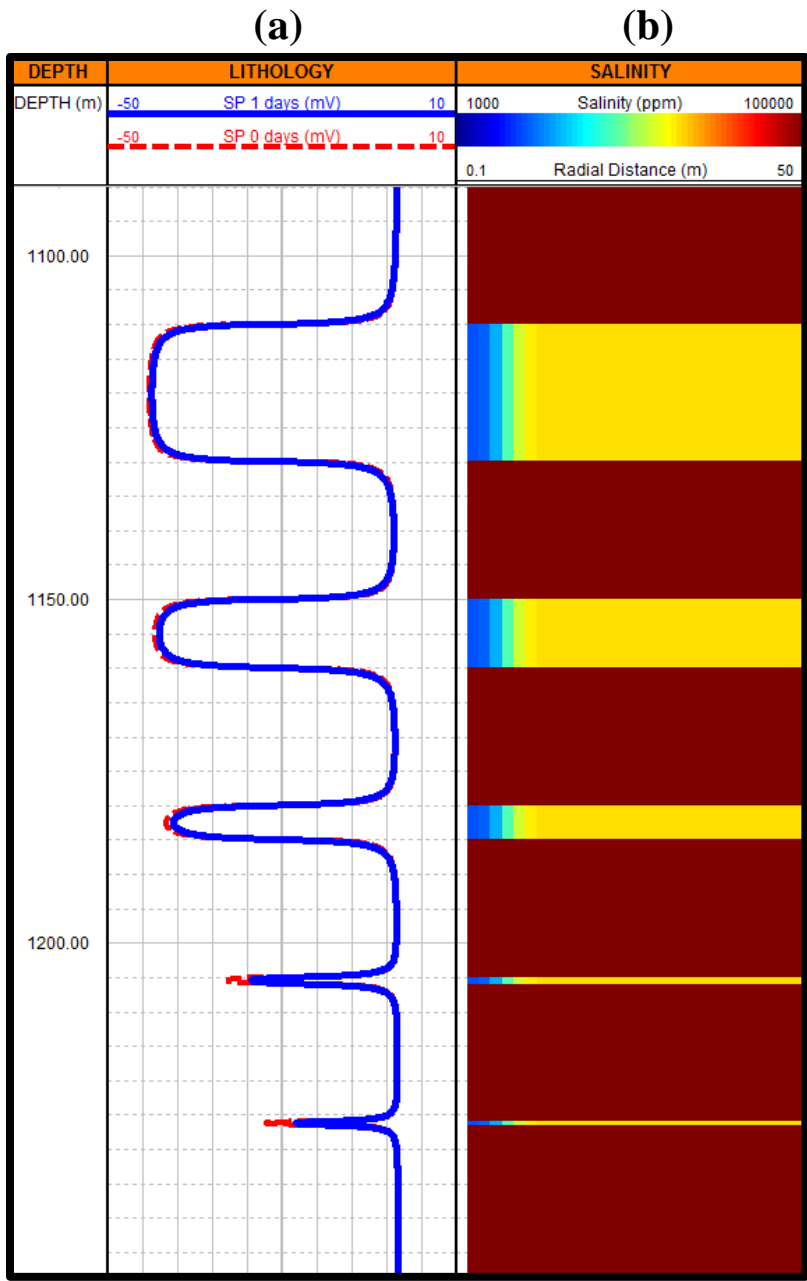


Figure 5.4: Track (a): Comparison of the SP log simulated across permeable beds with only a difference in their thickness. A comparison of the SP at 0 and 1 day after the onset of mud-filtrate invasion is presented to emphasize that invasion mainly affects the thinnest beds. Borehole size is 10 cm. Mud and formation water salinity are 3 kppm and 15 kppm. Temperature is set to 122 °F. Shales beds are perfect semi-permeable membranes. The second track shows the radial salinity profile after 1 day of invasion. All beds are water-bearing. Track (b): Salt concentration profile on that corresponds to mud-filtrate invasion after 1 day.

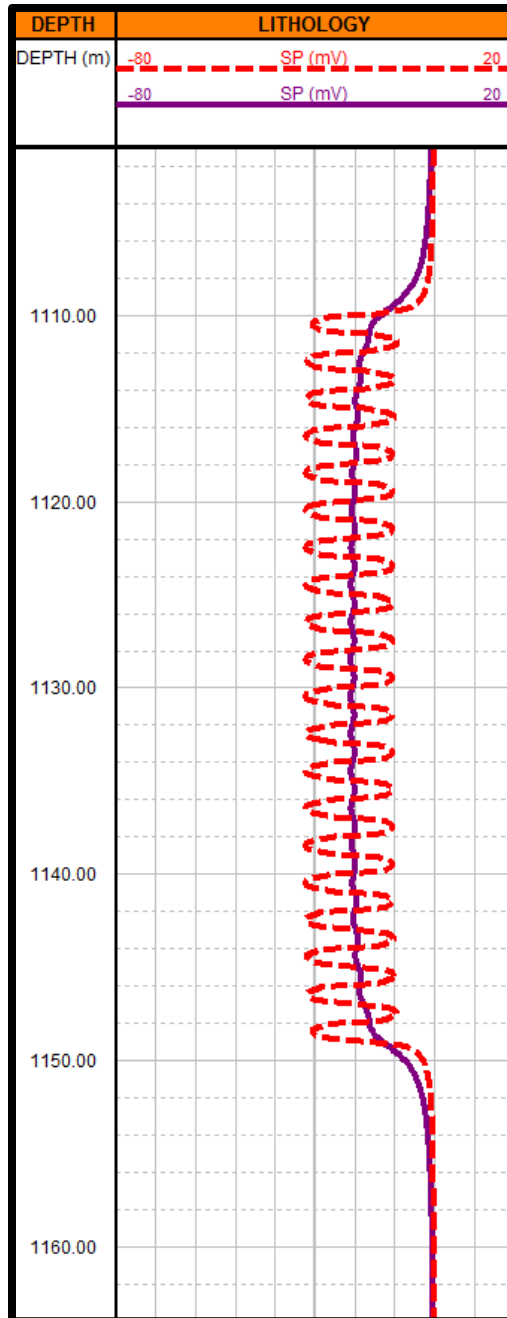


Figure 5.5: Averaging of SP log for thin-bedded formations. For the red SP log, the shale and non-shale beds are each 1 m thick, while for the purple SP log, the beds are each 10 cm thick. Both SP logs assume negligible mud-filtrate invasion. The temperature is set to 115 °F. All shale beds are assumed as perfect semi-permeable membranes. Borehole size is 10 cm. Mud and formation water salinity are 3 kppm and 15 kppm. All layers are water-bearing.

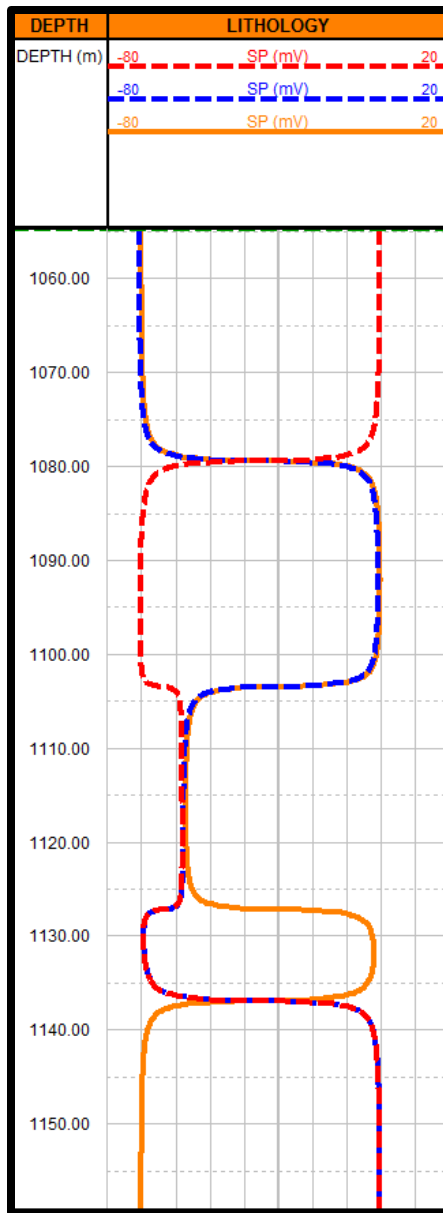


Figure 5.6: SP logs for different shale and sandstone configurations. A thick non-porous bed is located between 1,104 and 1,126 m in all configurations. Regardless of the arrangement of shale and sandstone beds, the SP log across the thick bed remains the same, which can be taken as an absolute baseline, given that no salt exchange occurs through it. All porous beds are water-bearing. The temperature is set to 122 °F. Mud salinity is 5 kppm and formation water salinity is 50 kppm in all cases. All examples assume no mud-filtrate invasion.

5.2 SHALE EFFECTS

Figure 5.7 compares an SP log calculated using Equation 3.4 ($Q_{vn} = 0.5$) for a laminated sandstone to the calculation made using individual sandstone and shale layers. EDL effects are assumed insignificant for this example. The results agree well, verifying the use of Equation 3.4 as an effective-medium model instead of having to simulate tens or hundreds of thin lamina. Although Equation 3.4 can be validated through simulations for laminated systems, this cannot be done for dispersed shale topologies. For this reason, experimental work to quantify the effect of dispersed shale on SP logs is currently underway. Results from these experiments will be reported in a future doctoral dissertation.

Figure 5.8 describes how the normalized SP log varies from 100% at the sandstone baseline to 0% at the shale baseline, as a function of volumetric shale content. The two different curves represent the SP logs acquired in the presence of laminated and dispersed shale topology, respectively. Both the laminated and dispersed topology can show nonlinear behavior with respect to fraction of clay, C_{sh} , depending on the value of Q_{vn} , which in turn depends on shale and non-shale porosities. For field work or automatic interpretation, the plots in Figure 5.8 can be generated and taken as reference for correcting SP logs in the field when data on volumetric concentration of shale and porosity are available.

5.2.1 Simulation of different shale ion permeabilities

The ability of a shale to allow the passage of only counterions (usually cations) is not only universal to all shales but also is quantifiable by using the proper equipment and samples (Al-Bazali *et al.*, 2005). From rig or laboratory measurements, it is clear that shales are not always perfect semi-permeable membranes, as they are often assumed to be (Al-Bazali *et al.*, 2005; Kerver and Prokop, 1957; Lomba *et al.*, 2000). Neglecting this behavior can bring detrimental consequences to calculations derived from SP logs.

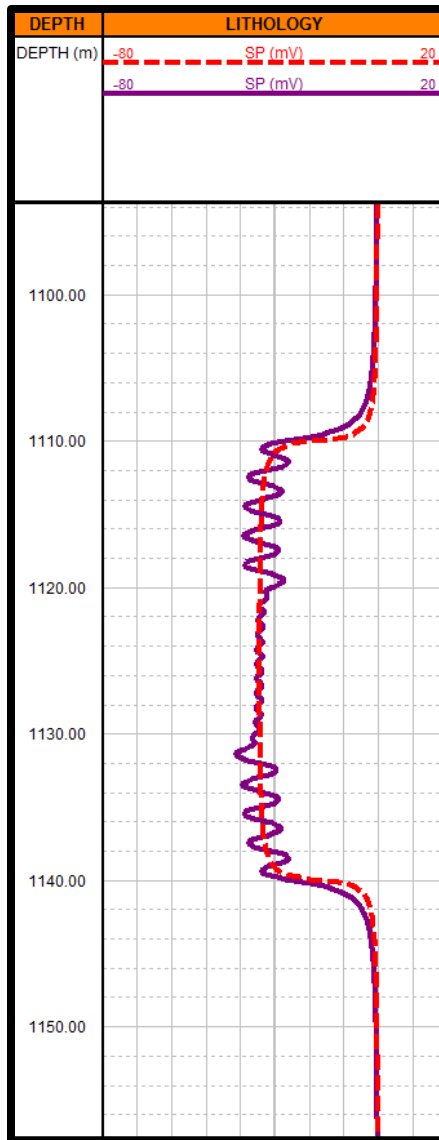


Figure 5.7: SP log calculated from individual non-shale and shale layers (purple log), and SP calculated from Eq. 3.4 for an effective medium (red log). As the thickness of individual layers decreases, the measured log converges to the effective log in red. The temperature is set to 122 °F. Mud salinity and formation water salinity are 5 kppm and 50 kppm, respectively. The borehole size is 10 cm. All layers are water-bearing only and assume no mud-filtrate invasion.

Figure 5.9 describes a simple example when two shale beds have different properties. The shale at the top has an ion permeability different from that of the bottom shale, giving rise to a shift in the shale baseline. Although such a shift is an indication of change of shale type, it can also be an indication of micro-fracturing, when both shales exhibit the same composition. Independent information can help to assess which case is true. However, having the SP log to initially recognize possible shale “leakage” can help to determine the integrity of the shale seal for trapping hydrocarbons or waste material stored underground (Gimmi and Kosakowski, 2011).

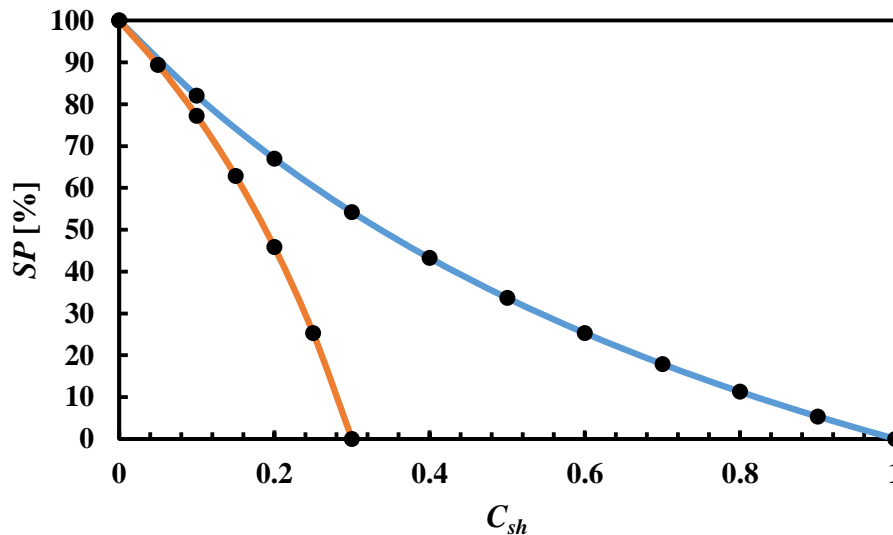


Figure 5.8: Normalized SP as a function of shale fraction (C_{sh}) for dispersed (red line) and laminated (blue line) shale topologies. The example plotted considers a rock with non-shale porosity of 0.3 and shale porosity of 0.15. In both cases, the relationship can be nonlinear with respect to C_{sh} . The calculations assume no mud-filtrate invasion.

5.3 HYDROCARBON EFFECTS

Figure 5.10 describes a case of one thick, non-shale bed containing hydrocarbon, displaying a continuous transition from $S_w = 100\%$ at the bottom to $S_w = S_{wirr}$ at the top.

Table 5.2 summarizes the properties assumed in the numerical simulation. Cases such as that shown in Figure 5.10 are reported by Doll (1949) and have been observed in several wells in Germany (Bautista-Anguiano and Torres-Verdín, 2015), which the author had the opportunity to analyze. With a smooth capillary transition with depth, the location of the oil-water contact (OWC) can be estimated from resistivity logs, but not necessarily from an SP log.



Figure 5.9: SP log for a non-shale porous bed rock shouldered by two different shale beds. The upper shale layer is simulated as a perfect semi-permeable membrane, while the lower shale layer is either as a highly laminated sandstone-shale sequence, a fractured shale, or a shale with different composition from the upper shale. Temperature is set to 122 °F. Mud and formation water salinities are 5 kppm and 50 kppm, respectively. For this figure, the transport numbers of sodium for the upper and lower shales are 1 and 0.8, respectively. All layers are only water-bearing and assume no mud-filtrate invasion.

In order to quantify hydrocarbon saturation from SP logs, a curve such as that shown in Figure 3.10 needs to be generated. This curve is a one-to-one relationship between SP and water saturation, from which the latter can be directly calculated from the SP log.

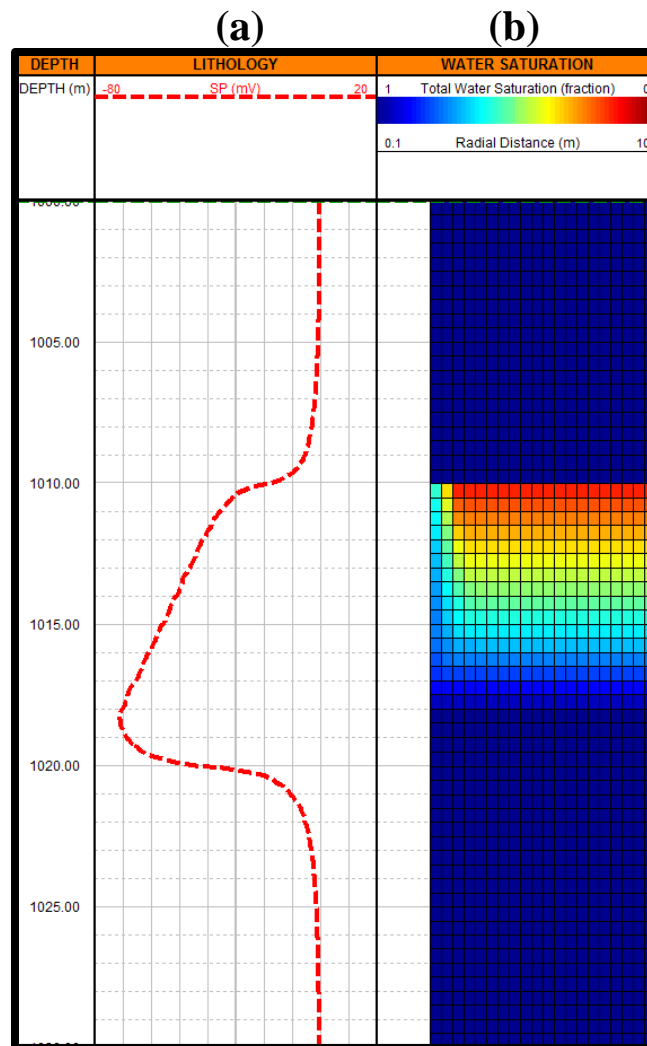


Figure 5.10: Track (a): Numerically simulated SP log with presence of hydrocarbon. The temperature is set to 120 °F. The mud and formation water salinities are 5 kppm and 50 kppm, respectively. Shales at the top and at the bottom are perfect semi-permeable membranes. The SP log is simulated with a mud-filtrate invasion time of 12 hours. The borehole radius is 10 cm. Track (b): Radial and vertical water-saturation distribution.

$D_{Na,bulk}$	$D_{Cl,bulk}$	$D_{Na,EDL}$	$D_{Cl,EDL}$	$S_{w,EDL}$
1×10^{-6} cm ² /s	1.54×10^{-6} cm ² /s	4×10^{-5} cm ² /s	1×10^{-8} cm ² /s	0.05

Table 5.2: Properties assumed for calculating effective ion diffusivities for the numerical simulation of SP log shown in Figure 5.10.

With a smooth capillary transition with depth, the location of the oil-water contact (OWC) can be estimated from resistivity logs, but not necessarily from an SP log.

5.3.1 Hydrocarbon effects on SP logs acquired across oil-wet rocks

Contrary to the SP effects observed in water-wet rocks, oil-wet rocks are not conventionally considered in SP interpretation. In order to assess the SP log acquired across this type of rocks, it is necessary to consider that because oil is in contact with the grains, no electrical double layer interacts with the ions in the water-phase, given that most non-organic ions dissolve only in water. Because of this behavior, the SP log will show no difference between a water-bearing reservoir and one containing hydrocarbons. Only at hydrocarbon saturations high enough to make the water a discontinuous phase or stored in the smallest pores is it possible to see any effect on the SP log. The latter effect is equivalent to having a non-porous rock in which no salt exchange takes place between the borehole and the rock. When an absolute reference can be set to identify these zones, the SP log can become a reliable qualitative tool in the identification of hydrocarbon zones. The advantage of such type of identification, from a production point of view, is that the reservoir will be produced with no or very low water cut.

5.4 SP LOG WITH DIFFERENT ELECTROLYTES

Than and Sprik (2016) document an attempt to quantify the effect that different ions have on the electrical double layer and, consequently, on the SP log. By comparing NaCl with Ca₂Cl, for example, Ca₂Cl can develop larger SP values than NaCl based solely

on diffusion, assuming that only one type of electrolyte is present in formation water. When more than one type of electrolyte is present in the mud and/or the formation water, it is necessary to consider the diffusivity of all ions present to define their respective transport numbers, as well as their concentrations, making the use of Equation 2.14 cumbersome. Future work is expected to help in the analysis of multi-ionic mixtures and their impact on the SP log; at present, all work presented here was performed assuming that only one cation and one anion are present in formation water and borehole mud.

CHAPTER 6: FIELD EXAMPLES OF THE QUANTITATIVE INTERPRETATION OF SP LOGS VIA NUMERICAL SIMULATION

This chapter documents two field examples used to test the numerical simulation of SP logs, honoring other logs available (i.e., nuclear and resistivity logs).

The first example is intended for the reconstruction of polarity inversion of an SP log in a German oil field, where no changes in salinity, clay content or porosity are present, but a sudden increase in electrical resistivity occurred. Here the presence of hydrocarbon suppresses the SP, inverting the deflection of the log.

The second case describes the behavior of the SP log with no deflection inversion as in the first example, but with a change in amplitude as hydrocarbon saturation increases, as indicated by resistivity and porosity logs. This example shows that, when the SP log is adequately calibrated, it can be used to reconstruct the vertical distribution of water saturation based only on the SP log. Interpretation results described for both scenarios are based on ion diffusivity values that are within a physically plausible range and that enable an adequate match between simulation and measurements.

6.1 FIELD CASE EXAMPLES

The SP numerical simulations for the field cases described above were done with a temperature of 52 °C. The bed of interest in both cases is clay free. For the first example, formation water and mud salt concentration are 85 kppm and 135,000 kppm, respectively. For the second example, formation water and mud salt concentrations are 85 kppm and 6 kppm, respectively. The borehole radius in both examples is 12 cm. In both cases, the simulation of SP is done with the salt concentration and water saturation distributions after 7 hours from the onset of mud-filtrate invasion. The parameters used to define the effective ion diffusivity and the effective transport numbers are indicated in the description of

Figures 6.1 and 6.2. Only the values of ion diffusivity at the EDL are mentioned. The values in bulk solution are the same as those shown in Table 3.2. Only NaCl is assumed to be present in the mud and formation water. The fraction of water associated with the EDL, $S_{w,EDL}$, is assigned a value of 0.05 in both examples. See Chapter 3 for details on the calculation of effective ion diffusivity and transport numbers.

6.1.1 Oil-water contact detection from SP log

The identification of oil-water contacts from SP logs has been studied for several decades since the works by Doll (1949, 1950). However, it was always assumed that in order for SP logs to sense the presence of hydrocarbons, presence of clay minerals was imperative (Coates and Miller, 1998). This field example, contrary to the conventional view, is clay free, but it senses the presence of hydrocarbons in the reservoir. From the theoretical framework presented in this report, it can be shown how the presence of hydrocarbons can have the effect observed in the field, and the phenomenon can be replicated with numerical simulations, as shown in Figure 6.1. Only the field logs and the numerical simulated SP are documented for this case. The next case, located in the same field, is shown in more detail, including a discussion of how the numerical match of all the logs available is achieved, as it was done for the case described in Figure 6.1.

6.1.2 SP log across a continuous capillary transition of water saturation

This second example (see Figure 6.2) shows, from resistivity and porosity logs, that hydrocarbon content increases upward. This phenomenon is reflected in the behavior of the SP log, which decreases in amplitude upward from the OWC (see Chapter 5, Figure 5.10), despite the fact that no changes in clay or porosity are sensed by the other logs. Hydrocarbon content is a possible explanation, as verified by the simulation results. SP logs are marginally affected by changes in porosity, and no changes in clay fraction are

sensed by the gamma-ray log. Additionally, this bed is thick enough to be marginally affected by mud-filtrate invasion or by the borehole radius. Hence, the presence of hydrocarbon is left as the only viable explanation of the behavior of the SP log in this example.

6.2 DISCUSSION

The numerical simulations in Figures 6.1 and 6.2 underscore the importance of developing a reliable SP simulator and indicate the need for conducting further research on this topic. These remaining issues are mentioned in the Chapter 7 of this report.

In reservoirs similar to that shown in Figure 6.1, a change in the polarity of the SP log may be regarded as an indicator of the presence of hydrocarbons. To determine the hydrocarbon pore volume, one must quantify ion diffusivity in the EDL for all ions present and calculate the volume of the EDL, according to Equation 3.4. This quantification, as shown in Figure 3.10, is necessary to determine the relationship of water saturation and SP voltage, allowing the petrophysicist to calculate the former directly from the latter.

In the second example, given that the logs belong to the same field as the first example, it was expected that similar properties in the EDL would yield reasonable results. As shown in Figure 6.2, an excellent match is obtained for the bed of interest. Hence, a calibration of the properties in the EDL from the first example would have enabled direct calculation of water saturation from the SP log of the second example without having to simulate the rest of the logs. In mature fields where SP and gamma-ray logs are the only information available, this capability to directly calculate water saturation from SP logs, based on a key well, is highly desirable. However, the calculation of properties in the EDL is a problem still under current research. Chapter 7 shows some potential solutions for resolving this problem.

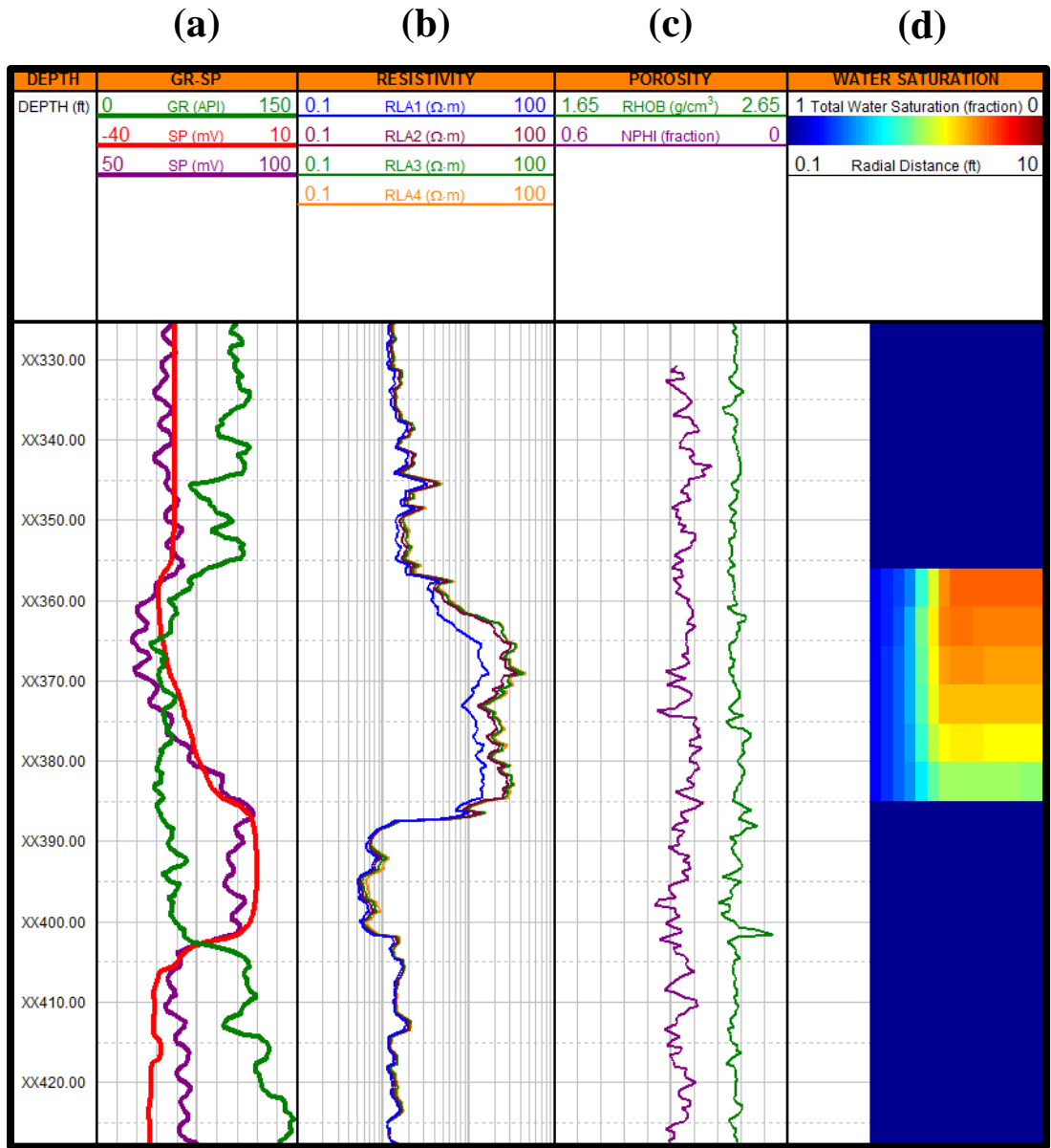


Figure 6.1: Track (a): Gamma-ray log in green, SP log in purple, and the numerically simulated SP log in red. The numerically simulated SP agrees with the SP log from the field. To achieve the match of the SP logs, the simulator used the properties $S_{w,EDL} = 0.05$, $D_{Na,EDL} = 8 \times 10^{-5} \text{ cm}^2/\text{s}$, and $D_{Cl,EDL} = 1 \times 10^{-10} \text{ cm}^2/\text{s}$ in the bed that extends from XX360 to XX405 ft. Track (b): Resistivity logs. Track (c): Density (green) and neutron (purple) logs. The neutron log is in limestone units. Track (d): Radial and vertical water-saturation distribution.

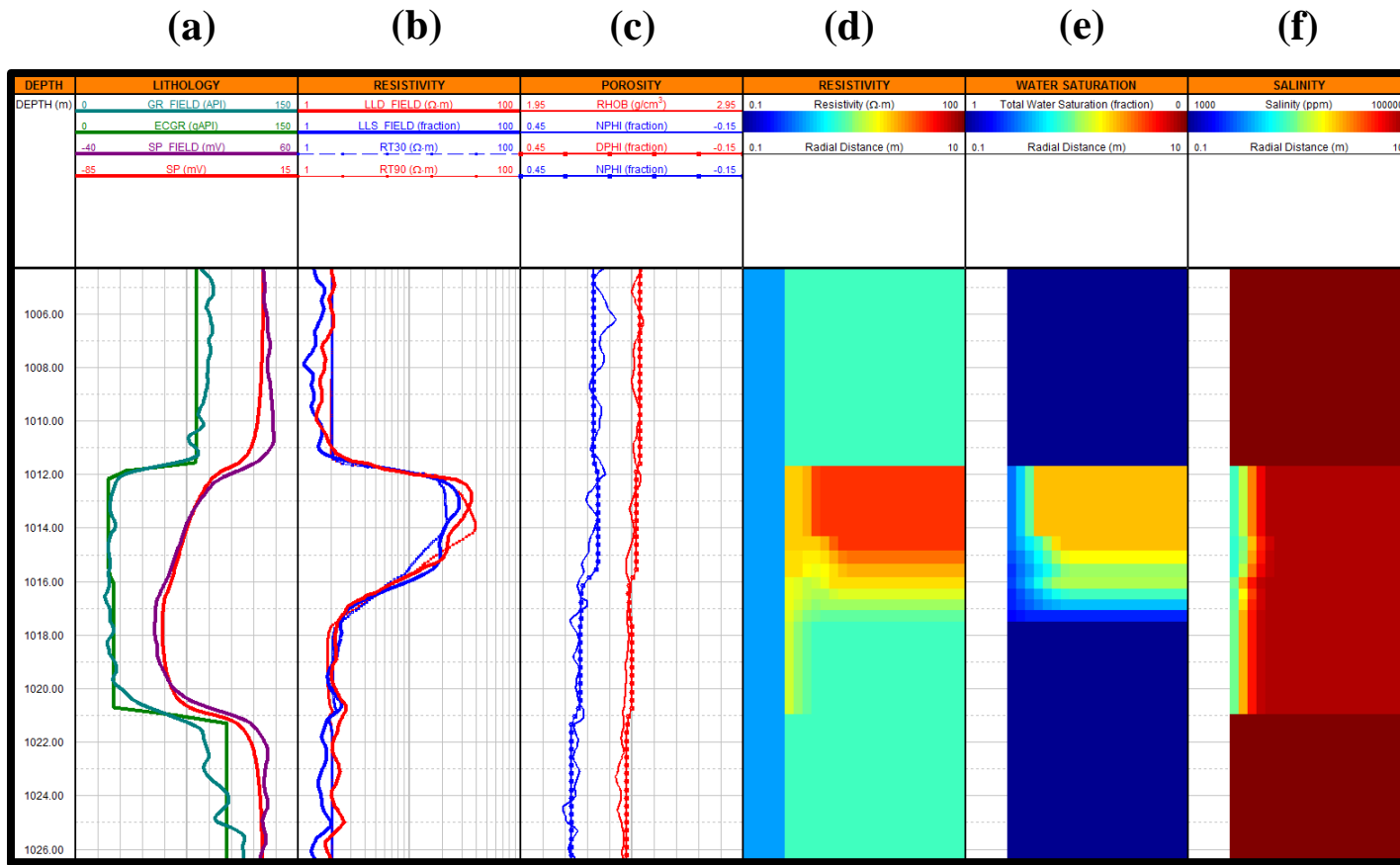


Figure 6.2: Track (a): Gamma-ray log with its simulated counterpart, both in green, and SP log in purple with the numerically simulated SP log in red. To achieve the match of the SP logs, the simulator used the properties $S_{w,EDL} = 0.05$, $D_{Na,EDL} = 8 \times 10^{-5} \text{ cm}^2/\text{s}$, and $D_{Cl,EDL} = 1 \times 10^{-10} \text{ cm}^2/\text{s}$ in the reservoir that extends from 1012 to 1021 m. Track (b): Resistivity logs (solid lines) and their simulated counterparts (dotted lines). Deep resistivity is in red, while shallow resistivity is in blue. Track (c): Density log in red and neutron log in blue. The numerical simulations of both logs are shown with dotted lines. The neutron log is in limestone units. Tracks (d), (e), and (f) are the resistivity, water saturation, and salt concentration radial profiles, respectively.

CHAPTER 7: CONCLUSIONS AND FUTURE WORK

7.1 CONCLUSIONS

Based on synthetic and field cases examined in the previous chapters, the SP log reveals its utility in the quantification of water saturation. This work, intended to establish and apply the physical principles behind the SP log in a mechanistic manner, successfully agrees with observations from the field.

Only seriously considered in the oil industry in recent decades, the electrical double layer plays a central role in all the results presented here. Without it, the SP log would provide no information as a petrophysical measurement. Without considering the presence and effects of the EDL, as was typically done in many previous publications, very little or no information on hydrocarbon pore volume could be extracted from SP logs.

Related to the EDL, the separation of the water phase in different diffusion domains (with different diffusivity values) is key in understanding why the SP is more or less sensitive to hydrocarbon content in water-wet rocks. At the same water-saturation value, different rocks could have different SP readings because their ion diffusion properties are different from one another. While the region away from the grain surfaces will be the same or very similar in most rocks, the region influenced by the double layer can be different, given that the surface chemistry and pore-size distribution of two rocks may not be the same, even though their general composition could be the same. This is a clear indication that SP logs are not only sensitive to the fluids present, but are also sensitive to the mineral composition of rock beds. This mineral composition determines the size and influence of the EDL in rock pores, which ultimately affects the SP reading in boreholes.

As explained in Chapter 5, Poisson's equation implicitly indicates that the electric potential at every point in the domain of interest is the result of the superposition principle.

Because of the validity of this principle, loss in vertical resolution is unavoidable. From this perspective, it is suggested that measuring SP logs with a centered tool has both advantages and disadvantages. As an advantage, the interpretation of the log is easier in asymmetric boreholes. However, at the center of the borehole the worst vertical resolution may exist because of the superposition of electric potential fields from different rock layers. If SP logs were measured on the borehole wall, the best vertical resolution possible and a clearer identification of bed boundaries would result.

The SP log across non-permeable formations is numerically simulated and found not to yield a linear SP log, as was suggested, but not proved, by previous work (Doll, 1949). Instead, these impermeable formations were found from the simulations to yield a baseline that can be regarded as an absolute zero in SP log interpretation. A zero baseline permits the identification of perfect membranes or the relevance of the electrokinetic component. This scenario requires further attention, involving study of field cases where non-permeable layers exist; such cases are not included in this report.

Shale ion permeability, always assumed to be that of a perfect semi-permeable membrane, is critical for a correct calibration and simulation of SP logs. It is advisable that, when possible, a verification of this permeability be made to make necessary adjustments in calculations derived from the SP log.

SP logs should be taken with the maximum salinity contrast possible. In freshwater-bearing rocks, salty mud should, when possible, be preferred over fresh mud. From Equation 2.14 it follows that SP depends on the logarithm of the salinity (concentration) ratio. If the salinity ratio is close to one, the SP log is close to zero. This ratio should be made as large as possible because it is not the ratio but its logarithm that is captured by the SP log. In practice, a ratio of 100 would be equivalent to a factor of 2 (under logarithm

with base 10). Hence, the salinity ratio is important when acquiring SP logs and should be adjusted, when possible, to yield good SP logs.

The electrokinetic component should be properly identified in all SP logs. This could be done by increasing or decreasing, within a secure operating window, the borehole pressure and comparing the SP measured at those pressures. Such a procedure could be a straightforward way to measure the factor $\frac{Q_v k}{\mu \sigma}$ in Equation 2.14. If independent measurements of viscosity, conductivity, and permeability are made, then it is possible to calculate Q_v and use it for proper calibration and simulation of SP logs. On the other hand, if Q_v is known, SP logs could be used to estimate permeability, as long as the electrokinetic component is significant and reliable.

With a SP-log simulator available, and using an adequate petrophysical model for electrochemical and electrokinetic SP, petrophysicists and other users can test their hypotheses of the configuration of the earth model being assessed. The highlight of this SP-log simulator is its use of Equation 2.14, which clearly proves that only the electrokinetic component depends on resistivity. This behavior simplifies the simulation and interpretation, because only one curve for thickness corrections and one curve for clay content are necessary, instead of several curves that depend on resistivity ratios (Doll, 1949) when the electrochemical component is dominant.

With a simplified interpretation, important properties such as porosity, permeability, hydrocarbon saturation, and water resistivity could be calculated from SP logs by following the recommendations provided in this thesis. In mature wells, such calculations may be challenging. If new wells are drilled in the same reservoir or if new wells are planned in the near future, the author advocates for conducting a proper SP characterization in these wells. Those wells, in turn used as key wells, can help in the interpretation of old SP logs and in making new discoveries at a low financial cost.

7.2 FUTURE WORK

Ion diffusivity, although significant in mass transport, is traditionally measured at infinite dilution. Even though useful for some applications, brine in mud and reservoirs is far from being at infinite dilution and is not composed of a single electrolyte. Because of this, new techniques need to be developed that allow the measurement of diffusivity at different concentrations with different mixtures of electrolytes found inside bed rocks. One of these techniques, and the most promising currently, is that of high-field NMR for ions (Holz, 1994; Pel *et al.*, 2016; Yang and Kausik, 2016) of sodium, chlorine, or potassium. Assuming that the NMR measurements can probe each ion, NMR assists in the quantification of the diffusivity of each ion present to correctly assign diffusivity values to each component in the bulk, the EDL, and the shale phases. With this technique, a major advancement in SP interpretation can be made, capable of calculating variable SP depending on specific rock properties, similar to pore-size or capillary pressure curves.

Electrokinetic SP, although neglected in traditional measurements, can be useful in cases where SP is related to fluid flow, such as flow in the reservoir or in fractures. Development of mechanistic models is underway and, just as with the electrochemical SP, such models could unveil useful information for reservoir interpretation.

Finally, although a 3D simulator is currently available, because it is based on finite differences it can be computationally demanding for conventional desktop computers. Parting from the example shown in Figure 5.4, if a 30-degree dip is added, keeping the same number of gridpoints in radial and depth directions as shown in Table 4, a CPU time of 20 minutes is needed to simulate the SP log numerically with 60 gridpoints in θ -direction. In future work, this simulator will be redesigned to reproduce SP logs from 3D models using a CPU time on the order of seconds. The goal is to promote the development of an inversion algorithm for SP logs, which is beyond the current scope of this project.

List of symbols

\bar{j}_i = mass flux	S_{wirr} = connate water saturation
\bar{j}_t = total charge current	V_p = pore volume
\hat{n}_r = vector normal to gridblock surface	a_i = activity of component i
$h_{eff,dip}$ = effective dip thickness	c_{\pm} = cation (+) or anion (-) concentration
C_{mf} = mud-filtrate water salinity	c_f = bulk solution ion concentration
C_w = formation water salinity	c_i = concentration of component i
$D_{i,eff}$ = effective diffusivity of ion i	f_i = fraction of capillaries with radius r_i
$D_{i,EDL}$ = ion diffusivity in EDL	\bar{r} = position vector
$D_{i,bulk}$ = ion diffusivity in bulk solution	r_i = radius for capillary i
$D_{i,clay}$ = ion diffusivity in clay	r_{bh} = borehole radius
D_i = diffusivity of component i	r_{inv} = mud-filtrate invasion radius
D_o = bulk solution diffusivity	t_i = transport number of ion i
Q_v = excess charge per pore volume	θ_{dip} = dip
Q_{vn} = normalized Q_v	v_{EDL} = volume fraction of EDL
R_{mf} = mud-filtrate resistivity	v_{bulk} = volume fraction of bulk solution
R_w = formation water resistivity	v_{clay} = volume fraction of clay
$S_{w,EDL}$ = water fraction with EDL	ρ_{dry} = density of dry clay
$S_{w,free}$ = water fraction free from EDL	ϵ_f = electrical permittivity

C_{sh} = clay fraction

k = permeability

F = Faraday's constant

z = ion valence

h = thickness

α = factor for logarithmic spacing

h_{norm} = normalized thickness

ζ = EDL electric potential

R = gas constant

κ = inverse of EDL thickness

T = temperature

λ = EDL thickness

CEC = cation-exchange capacity

μ = fluid viscosity

K = coefficient in *SSP* definition

σ = electrical conductivity

P = pressure

τ = tortuosity

S = mineral surface area

ϕ = porosity

SSP = static SP

V = spontaneous potential

List of acronyms

EDL = Electric Double Layer

NMR = Nuclear Magnetic Resonance

OWC = Oil-water contact

SP = Spontaneous Potential

UTAPWeLS = University of Texas at Austin Petrophysical and Well-Logging Simulator

References

- Ahmad MU, 1964, "A laboratory study of streaming potentials", *Geophysical Prospecting* 12(1): 49–64, DOI: 10.1111/j.1365-2478.1964.tb01889.x.
- Al-Bazali TM, Zhang J, Chenevert ME, and Sharma MM, 2005, "A rapid, rigsite deployable, electrochemical test for evaluating the membrane potential of shales", paper presented at the Annual Technical Conference and Exhibition, Society of Petroleum Engineers: Dallas, Texas, DOI: 10.2118/96098-MS.
- Allègre V, Jouniaux L, Lehmann F, and Sailhac P, 2010, "Streaming potential dependence on water-content in Fontainebleau sand", *Geophysical Journal International* 182(3): 1248–1266, DOI: 10.1111/j.1365-246X.2010.04716.x.
- Archie GE, 1942, "The electrical resistivity log as an aid in determining some reservoir characteristics", *Transactions of the AIME* 146(1): 54–62, DOI: 10.2118/942054-G.
- Bautista-Anguiano J and Torres-Verdín C, 2015, "Mechanistic Description, Simulation, and Interpretation of Spontaneous Potential Logs", paper presented at the SPWLA 56th Annual Logging Symposium, Society of Petrophysicists and Well-Log Analysts: Long Beach, California.
- Bolève A, Revil A, Janod F, Mattiuzzo JL, and Jardani A, 2007, "Forward Modeling and validation of a new formulation to compute self-potential signals associated with ground water flow", *Hydrology and Earth System Sciences* 11(5): 1661–1671, DOI: 10.5194/hess-11-1661-2007.
- Bringuier E, 2013, "The Maxwell–Stefan description of binary diffusion", *European Journal of Physics* 34(5): 1103, DOI: 10.1088/0143-0807/34/5/1103.
- Clavier C, Coates G, and Dumanoir J, 1984, "Theoretical and experimental bases for the dual-water model for interpretation of shaly sands", *Society of Petroleum Engineers Journal* 24(2): 153–168, DOI: 10.2118/6859-PA.
- Coates GR and Miller D, 1998, "Using NMR logs to reconstruct SP and confirm R_w ", *The Log Analyst* 39(3): 58–65.
- Daiguji H, 2010, "Ion transport in nanofluidic channels", *Chemical Society Reviews* 39(3): 901–911, DOI: 10.1039/B820556F.
- Dakhnov VN, 1962, "Geophysical well logging", Quarterly of The Colorado School of Mines: Golden, Colorado.

- Darnet M and Marquis G, 2004, "Modelling streaming potential (SP) signals induced by water movement in the vadose zone", *Journal of Hydrology* 285(1–4): 114–124, DOI: 10.1016/j.jhydrol.2003.08.010.
- De Andrade PV, 1955, "A result of SP log interpretation", *Journal of Petroleum Technology* 7(11): 59–60, DOI: 10.2118/468-G.
- Dickey PA, 1944, "Natural potentials in sedimentary rocks", *Transactions of the AIME* 155(1): 39–48, DOI: 10.2118/944039-G.
- Doll HG, 1949, "The SP log: Theoretical analysis and principles of interpretation", *Transactions of the AIME* 179(1): 146–185, DOI: 10.2118/949146-G.
- Doll HG, 1950, "The SP log in shaly sands", *Journal of Petroleum Technology* 2(7): 205–214, DOI: 10.2118/950205-G.
- Eijkel JCT and van den Berg A, 2010, "Nanofluidics and the chemical potential applied to solvent and solute transport", *Chemical Society Reviews* 39(3): 957, DOI: 10.1039/b913776a.
- Ellis DV and Singer JM, 2007, "*Well logging for Earth scientists*", Springer Netherlands.
- Gimmi T and Kosakowski G, 2011, "How mobile are sorbed cations in clays and clay rocks?", *Environmental Science & Technology* 45(4): 1443–1449, DOI: 10.1021/es1027794.
- Glowinski R, Rouault GF, and Tabanou JR, 1988, "SP deconvolution and quantitative interpretation in shaly sands", *The Log Analyst* 29(5): 332–344.
- Hamann CH, Hamnett A, and Vielstich W, 2007, "*Electrochemistry*", Wiley: Germany.
- Hill HJ and Anderson AE, 1959, "Streaming potential phenomena in SP log interpretation", *Petroleum Transactions, AIME* 216(1): 203–208.
- Hill HJ and Milburn JD, 1956, "Effect of clay and water salinity on electrochemical behavior of reservoir rocks", *Petroleum Transactions, AIME* 207(1): 65–72.
- Holz M, 1994, "Electrophoretic NMR", *Chemical Society Reviews* 23(3): 165–174.
- Juhasz I, 1981, "Normalised Qv - The key to shaly sand evaluation using the Waxman-Smits equation in the absence of core data", paper presented at the SPWLA 22nd Annual Logging Symposium, Society of Petrophysicists and Well-Log Analysts: Mexico City, Mexico.

Kärger J and Valiullin R, 2011, "Diffusion in porous media", *Encyclopedia of Magnetic Resonance*, John Wiley & Sons, Ltd: Chichester, UK, 1–14.

Kerver JK and Prokop CL, 1957, "Effect of the presence of hydrocarbons on well logging potential", paper presented at the Annual Fall Meeting of the Southern California Petroleum Section of the American Institute of Mining, Metallurgical and Petroleum Engineers, AIME: Los Angeles, California.

Koryta J, Dvorak J, and Kavan L, 1994, "*Principles of Electrochemistry*", Wiley: England.

Krishna R and van Baten JM, 2009, "Unified Maxwell–Stefan description of binary mixture diffusion in micro- and meso-porous materials", *Chemical Engineering Science* 64(13): 3159–3178, DOI: 10.1016/j.ces.2009.03.047.

Krishna R and Wesselingh JA, 1997, "The Maxwell-Stefan approach to mass transfer", *Chemical Engineering Science* 52(6): 861–911, DOI: 10.1016/S0009-2509(96)00458-7.

Lehikoinen J, Muurinen A, and Valkiainen M, 1999, "A consistence model for anion exclusion and surface diffusion", *MRS Online Proceedings Library Archive* 556, DOI: 10.1557/PROC-556-663.

Leinov E and Jackson MD, 2014, "Experimental measurements of the SP response to concentration and temperature gradients in sandstones with application to subsurface geophysical monitoring", *Journal of Geophysical Research: Solid Earth* 119(9): 2014JB011249, DOI: 10.1002/2014JB011249.

Lomba RFT, Chenevert ME, and Sharma MM, 2000, "The ion-selective membrane behavior of native shales", *Journal of Petroleum Science and Engineering* 25(1–2): 9–23, DOI: 10.1016/S0920-4105(99)00028-5.

Malik M, Salazar JM, Torres-Verdin C, Wang GL, Lee HJ, and Sepehrnoori K, 2008, "Effects of Petrophysical Properties On Array-Induction Measurements Acquired In the Presence of Oil-Base Mud-Filtrate Invasion1", *Petrophysics* 49(1).

McCall C, Von Genten WD, and Osoba JS, 1971, "The effect of hydrocarbons on the SP opposite sands", paper presented at the SPWLA 12th Annual Logging Symposium, Society of Petrophysicists and Well-Log Analysts: Dallas, Texas.

McCardell WM, Winsauer WO, and Williams M, 1953, "Origin of the electric potential observed in wells", *Journal of Petroleum Technology* 5(2): 41–50, DOI: 10.2118/215-G.

Mitchell JK, 1991, "Conduction phenomena: from theory to geotechnical practice", *Géotechnique* 41(3): 299–340, DOI: 10.1680/geot.1991.41.3.299.

Mounce WD and Rust WM, 1944, "Natural potentials in well logging", *Transactions of the AIME* 155(1): 49–57, DOI: 10.2118/944049-G.

Ortiz IJ, Von Genten WD, and Osoba JS, 1972, "Relationship of the electrochemical potential of porous media with hydrocarbon saturation", paper presented at the SPWLA 13th Annual Logging Symposium, Society of Petrophysicists and Well-Log Analysts: Tulsa, Oklahoma.

Pel L, Donkers PAJ, Kopinga K, and Noijen JJ, 2016, "¹H, ²³Na and ³⁵Cl imaging in cementitious materials with NMR", *Applied Magnetic Resonance* 47(3): 265–276, DOI: 10.1007/s00723-015-0752-6.

Poupon A, Loy ME, and Tixier MP, 1954, "A contribution to electrical log interpretation in shaly sands", *Journal of Petroleum Technology* 6(6): 27–34, DOI: 10.2118/311-G.

Revil A, 1999, "Ionic diffusivity, electrical conductivity, membrane and thermoelectric potentials in colloids and granular porous media: A unified model", *Journal of Colloid and Interface Science* 212(2): 503–522, DOI: 10.1006/jcis.1998.6077.

Revil A, Cathles LM, Losh S, and Nunn JA, 1998, "Electrical conductivity in shaly sands with geophysical applications", *Journal of Geophysical Research: Solid Earth* 103(B10): 23925–23936, DOI: 10.1029/98JB02125.

Revil A and Jougnot D, 2008, "Diffusion of ions in unsaturated porous materials", *Journal of Colloid and Interface Science* 319(1): 226–235, DOI: 10.1016/j.jcis.2007.10.041.

Revil A and Leroy P, 2004, "Constitutive equations for ionic transport in porous shales", *Journal of Geophysical Research: Solid Earth* 109(B3): B03208, DOI: 10.1029/2003JB002755.

Saad Y, 2003, "*Iterative methods for sparse linear systems*", Society for Industrial and Applied Mathematics: Philadelphia, Pennsylvania.

Salazar J, Li Wang G, Torres-Verdín C, and Lee HJ, 2008, "Combined simulation and inversion of SP and resistivity logs for the estimation of connate-water resistivity and Archie's cementation exponent", *Geophysics* 73(3): E107–E114, DOI: 10.1190/1.2890408.

Salazar JM and Torres-Verdín C, 2009, "Quantitative comparison of processes of oil- and water-based mud-filtrate invasion and corresponding effects on borehole resistivity measurements", *Geophysics* 74(1): E57–E73, DOI: 10.1190/1.3033214.

Saunders JH, Jackson MD, and Pain CC, 2006, "A new numerical model of electrokinetic potential response during hydrocarbon recovery", *Geophysical Research Letters* 33(15): L15316, DOI: 10.1029/2006GL026835.

Schlumberger C, Schlumberger M, and Leonardon EG, 1934, "Electrical coring: A method of determining bottomhole data by electrical measurements", *Transactions of the AIME* 110(1): 237–272, DOI: 10.2118/934237-G.

Segesman F, 1962, "New SP correction charts", *Geophysics* 27(6): 815–828, DOI: 10.1190/1.1439106.

Segesman F and Tixier MP, 1959, "Some effects of invasion on the SP curve", *Petroleum Transactions, AIME* 216(1): 138–146.

Settari A and Aziz K, 1972, "Use of irregular grid in reservoir simulation", *Society of Petroleum Engineers Journal* 12(2): 103–114, DOI: 10.2118/3174-PA.

Sill W, 1983, "Self-potential modeling from primary flows", *Geophysics* 48(1): 76–86, DOI: 10.1190/1.1441409.

Stallmach F and Kärger J, 1999, "The potentials of pulsed field gradient NMR for investigation of porous media", *Adsorption* 5(2): 117–133.

Strikwerda J, 2004, "*Finite difference schemes and partial differential equations*", Society for Industrial and Applied Mathematics: Pacific Grove, California.

Tatsien L, Yongji T, and Yuejun P, 1994, "Mathematical model and method for spontaneous potential well-logging", *European Journal of Applied Mathematics* 5(2): 123–139, DOI: 10.1017/S0956792500001352.

Thanh L and Sprik R, 2016, "Zeta potential in porous rocks in contact with monovalent and divalent electrolyte aqueous solutions", *Geophysics* 81(4): D303–D314, DOI: 10.1190/geo2015-0571.1.

van der Vorst H, 1992, "Bi-CGSTAB: A fast and smoothly converging variant of Bi-CG for the solution of nonsymmetric linear systems", *SIAM Journal on Scientific and Statistical Computing* 13(2): 631–644, DOI: 10.1137/0913035.

Vasconcelos S, Mendonça C, and Silva N, 2014, "Self-potential signals from pumping tests in laboratory experiments", *Geophysics* 79(6): EN125-EN133, DOI: 10.1190/geo2013-0444.1.

Voss B, Torres-Verdin C, Gandhi A, Alabi G, and Lemkecher M, 2009, "Common Stratigraphic Framework To Simulate Well Logs And To Cross-Validate Static And Dynamic Petrophysical Interpretations", paper presented at the SPWLA 50th Annual Logging Symposium, Society of Petrophysicists and Well-Log Analysts: The Woodlands, Texas.

Winsauer WO and McCardell WM, 1953, "Ionic double-layer conductivity in reservoir rock", *Journal of Petroleum Technology* 5(5): 129–134, DOI: 10.2118/953129-G.

Woodruff WF, Revil A, Jardani A, Nummedal D, and Cumella S, 2010, "Stochastic Bayesian inversion of borehole self-potential measurements", *Geophysical Journal International* 183(2): 748–764, DOI: 10.1111/j.1365-246X.2010.04770.x.

Wyllie MRJ, 1949, "A quantitative analysis of the electrochemical component of the SP curve", *Journal of Petroleum Technology* 1(1): 17–26, DOI: 10.2118/949017-G.

Wyllie MRJ and Southwick PF, 1954, "An experimental investigation of the SP and resistivity phenomena in dirty sands", *Journal of Petroleum Technology* 6(2): 44–57, DOI: 10.2118/302-G.

Yang D and Kausik R, 2016, "²³Na and ¹H NMR relaxometry of shale at high magnetic field", *Energy & Fuels* 30(6): 4509–4519, DOI: 10.1021/acs.energyfuels.6b00130.

Vita

Joshua Christopher Bautista-Anguiano was born in Mexico. He joined the National Autonomous University of Mexico (UNAM) in the Geophysical Engineering Program in 2008. After successfully graduating in August 2013, he entered the Graduate School of The University of Texas at Austin in January 2014.

E-mail address: joshuabau@gmail.com

This report was typed by the author.